

Real-time Range-Angle Estimation and Tag Localization for Multi-static Backscatter Systems

Tara Esmaeilbeig*, Kartik Patel*, Traian E. Abrudan, John Kimionis, Eleftherios Kampianakis, Michael Eggleston

Abstract—Multi-static backscatter networks (BNs) are strong candidates for joint communication and localization in the ambient IoT paradigm for 6G. Enabling real-time localization in large-scale multi-static deployments with thousands of devices require highly efficient algorithms for estimating key parameters such as range and angle of arrival (AoA), and for fusing these parameters into location estimates. We propose two low-complexity algorithms, Joint Range-Angle Clustering (JRAC) and Stage-wise Range-Angle Estimation (SRAE). Both deliver range and angle estimation accuracy comparable to FFT- and subspace-based baselines while significantly reducing the computation. We then introduce two real-time localization algorithms that fuse the estimated ranges and AoAs: a maximum-likelihood (ML) method solved via gradient search and an iterative re-weighted least squares (IRLS) method. Both achieve localization accuracy comparable to ML-based brute force search albeit with far lower complexity. Experiments on a real-world large-scale multi-static testbed with 4 illuminators, 1 multi-antenna receiver, and 100 tags show that JRAC and SRAE reduce runtime by up to $40\times$ and IRLS achieves up to $500\times$ reduction over ML-based brute force search without degrading localization accuracy. The proposed methods achieve 3 m median localization error across all 100 tags in a sub-6GHz band with 40 MHz bandwidth. These results demonstrate that multi-static range-angle estimation and localization algorithms can make real-time, scalable backscatter localization practical for next-generation ambient IoT networks.

Index Terms—Backscatter, integrated communications and sensing, Joint range and angle estimation, IoT.

I. Introduction

The ambient IoT paradigm envisioned for 6G demands large-scale connectivity and sensing solutions powered by ultra-low energy devices. Backscatter communication is a strong candidate to realize this vision [1]–[3]. While early commercial backscatter systems, based on monostatic architectures [4], were constrained by short range and limited scalability, the recent advances in ambient and multi-static backscatter architectures overcome these limitations and support wide-area deployments while retaining the low-power benefits of backscatter devices [5]–[9].

Prior art has proven the feasibility of multi-static and ambient backscatter networks (BNs) for communication with focus on data transmission and network scalability [10]–[20], with few examples exploring localization capabilities in sub-6GHz systems [21]–[23]. Multi-static

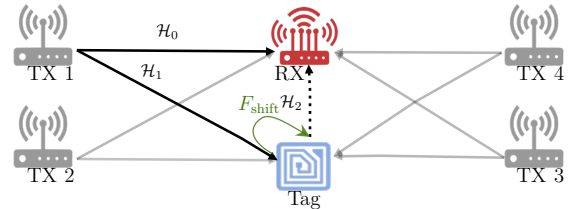


Fig. 1. An illustration of a multi-static BN comprising 4 TXs, 1 multi-antenna RX, and a frequency-shifting tag: The tag shifts the carrier signal to an adjacent band to allow the RX process both signals simultaneously, and enable the bistatic range-angle estimation without external synchronization. Combining range-angle estimates from multiple TX-RX-pairs enable tag localization.

localization is critical for applications like asset tracking and context-aware IoT, manifesting a demand for scalable architectures and algorithms that jointly support communication and localization.

In this work, we introduce a multi-static BN designed to natively support localization of tags. As illustrated in Fig. 1, the network consists of multiple single-antenna transmitters (TXs), multi-antenna receivers (RXs), and frequency-shifting backscatter tags [10]. By shifting and reflecting the incident carrier to an adjacent band, each tag enables the RX to process the direct and backscattered signals simultaneously. This dual-band processing (a) isolates the backscatter signal from strong direct-path interference, and (b) allows time-difference of arrival (TDoA)-based bistatic ranging using the direct TX signal as a timing without external synchronization between TXs and RXs. Furthermore, multi-antenna RXs support angle-of-arrival (AoA) estimation from the backscatter signal.

We first develop bistatic range-angle estimation algorithms tailored for this architecture. Although range-angle estimation using wideband multi-antenna channels has been extensively studied [24], [25], scalable solutions suitable for networks with hundreds of tags remain an open challenge. To address this, we propose two methods: (a) Joint Range-Angle Clustering (JRAC) which is a joint estimator that clusters dominant multipath components in a truncated range-angle heatmap. (b) Stage-wise Range-Angle Estimation (SRAE) which is a decoupled approach that estimates range and angle sequentially. Compared to conventional approaches like 2D FFT [24] and 2D MUSIC [25] that incur prohibitive computational complexity, JRAC and SRAE achieve near real-time operations without sacrificing accuracy.

Beyond estimation, we develop two real-time multi-static localization algorithms that fuse range and angle

* Two authors have equal contributions. All authors are with Nokia Bell Labs. Email addresses: tara.esmaeilbeig@nokia.com, {kartik.patel, traian.abrudan, ioannis.kimionis, lefteris.kampianakis, michael.eggleston} @nokia-bell-labs.com

estimates: (a) an ML-based localization solved using gradient ascent-based algorithm with line search, and (b) an iterative re-weighted least squares (IRLS) method that delivers comparable accuracy with dramatically lower computational costs.

Finally, we validate our methods on a large-scale real-world testbed comprising 4 TXs, 1 RX, and 100 semi-passive tags deployed in a 20×7 m indoor area. Despite heavy multipath conditions, our proposed algorithms achieve positioning accuracy comparable to baselines while reducing runtime by orders of magnitude. These results demonstrate the practicality of multi-static BNs for integrated communication and localization in next-generation ambient IoT networks.

A. Prior Art

1) Real-world Multi-static Localization Systems: Recent BNs commonly adopt multi-static or ambient backscatter architectures for communication [12]–[20]. However, only a few works demonstrate real-world localization using multi-static architectures in sub-6 GHz bands [21]–[23]. Work in [21] estimates direction-of-arrival and localizes RFID tags with a multistatic setup that requires a wired shared clock between radios. The latter, though effective for synchronization of co-located nodes, adds an element of deployment complexity for sparse, wide-area installations. Additionally, interference from multiple transmitters may become significant when TX and RX antennas are not co-linear, due to backscattering occurring in same channel. In contrast, our system leverages frequency-shifted backscatter, eliminating the need for external synchronization and reducing TX-induced interference. Alternatively, [22] estimates bistatic ranges using received signal strength (RSS) measurements combined with particle-filter-based localization, which is appealing as a narrowband scheme. Our approach uses wideband signaling for illumination and phase-based ranging, which is more favorable in multipath environments [26], due to the full channel sounding characteristics. Finally, [23] introduces digital TX-interference cancellation for in-band tag reflections. In our approach, by using frequency-shifting tags, we eliminate the need for such interference cancellation schemes, maximizing the receiver dynamic range independently for the illumination and backscatter signals, respectively.

2) Joint Range-Angle Estimation: There are two main approaches for joint range-angle estimation. The first constructs a 2D range-angle heatmap and exploits structural assumptions to recover the Line of Sight (LoS) path. For example, compressive-sensing methods assume sparsity in the range-angle domain to search for the LoS component efficiently [27], [28]. However, operating in the sub-6 GHz bands with less than 40 MHz bandwidth limits the sparsity in our setup, making such approaches less effective. The second class of methods, such as 2D FFT [24] and 2D MUSIC [25], [29], compute the range-angle heatmap on a quantized grid and identify LoS peaks through max-peak

detection or iterative refinement, as in [23]. Although accurate, these methods incur high computational cost due to dense grid evaluations. Our proposed JRAC and SRAE algorithms optimize this class of methods by truncating the grid search and using stage-wise range-angle estimation, resulting in substantial runtime reduction with minimal loss in accuracy.

3) Localization Techniques: We model errors in AoA measurements using directional statistics [30]. Since the angles are inherently periodic, they lie on a circular or spherical manifold rather than in Euclidean space. As a result, widely used statistical distributions are not representative of the angular errors. To the best of our knowledge, directional statistics were first applied to AoA-based localization using von Mises–Fisher distribution in [31], and using von Mises distribution in [32], [33]. Subsequently, maximum likelihood (ML) based localization with Time-of-Arrival (ToA) measurements was introduced in [34], [35] for active-radio localization systems, which was later extended to incorporate joint range and angle measurements in [36]. In this paper, we extend this ML-based formulation to the multistatic setting and develop a gradient ascent algorithm with line search for efficiently estimating the tag position.

Our second method, IRLS, is inspired by the pseudo-linear formulation for bi-static localization introduced in [37]. Follow-up work applied similar ideas to active-radio settings with range-only measurements [38]–[40] and AoA-only measurements [41]. In this paper, we extend IRLS to use both range and AoA measurements in a multi-static BN. Drawing from our experimental observations, we further refine the IRLS procedure to ensure robustness in practical deployments.

Lastly, [42], [43] derive Cramer-Rao Lower Bound (CRLB) for multi-static localization but do not provide algorithms to achieve those limits. Moreover, temporal filtering techniques such as Kalman or particle filters can further improve localization performance [22], [44]. In this paper, we focus on raw localization performance, without exploring filtering, and assume that the localization accuracy can be further improved using subsequent filtering.

B. Summary of Contributions

In summary, the contributions of this paper are as follows:

- We introduce a multi-static BN that natively supports tag localization along with communication, without any synchronization between TXs and RXs. The system uses the direct carrier signal as a timing reference for bistatic ranging and uses multi-antenna RXs for AoA estimation.
- We present two efficient algorithms, JRAC and SRAE, for joint range-angle estimation in a bistatic backscatter system. We show these methods are computationally efficient without sacrificing the estimation accuracy.
- We develop two localization algorithms that fuse bistatic range and angle. First, we formulate an

ML estimator assuming Gaussian range errors and von Mises–Fisher distributed angular errors, and solve it via gradient ascent with line search. Second, we introduce an IRLS-based method using pseudo-linear formulation. We show that both of these methods significantly reduce runtime while preserving overall localization performance.

- We build a large-scale experimental testbed and collect two datasets: (a) with a 4-tag setup representing a simplified scenario, and (b) with a 100-tag setup representing a dense practical deployment. Using these datasets, we evaluate our estimation and localization methods, analyze their computation complexity (and runtime), and highlight key empirical observations on the challenging wireless environment data.

II. System Model

A. System Setup

The multi-static BN consists of N_{TX} TXs and N_{RX} RXs located in D -dimensional space, $D \in \{2, 3\}$. We denote the position of the i -th TX by $\mathbf{p}_{\text{TX},i}$, j -th RX by $\mathbf{p}_{\text{RX},j}$, and a backscatter tag by \mathbf{p} .

We denote by $d_{\mathbf{B}}^{(i,j)}$ the distance between i -th TX and j -th RX. We further define the bistatic range as the distance traveled by a signal from i -th TX to j -th RX via the tag. Denoting the bistatic range by $d_{\mathbf{B}}^{(i,j)}$, we have

$$d_{\mathbf{B}}^{(i,j)} = \|\mathbf{p} - \mathbf{p}_{\text{TX},i}\| + \|\mathbf{p} - \mathbf{p}_{\text{RX},j}\|. \quad (1)$$

Let the angular position of the TX and the tag, i.e., AoA of the carrier and the backscatter signals, w.r.t. the j -th receiver denoted by $(\theta_0^{(i,j)}, \phi_0^{(i,j)})$, $(\theta_2^{(j)}, \phi_2^{(j)})$, where $\theta_0^{(i,j)}, \theta_2^{(j)} \in [-\pi, \pi]$ denote the azimuthal angles and $\phi_0^{(i,j)}, \phi_2^{(j)} \in [0, \pi]$ denote the elevation angles. Then,

$$\frac{\mathbf{p} - \mathbf{p}_{\text{RX},j}}{\|\mathbf{p} - \mathbf{p}_{\text{RX},j}\|} = \left[\sin \phi_2^{(j)} \cos \theta_2^{(j)}, \sin \phi_2^{(j)} \sin \theta_2^{(j)}, \cos \phi_2^{(j)} \right]^{\top}. \quad (2)$$

In this work, we are interested in

- estimating $(d_{\mathbf{B}}^{(i,j)}, \theta_2^{(j)}, \phi_2^{(j)})$ from the carrier and the backscatter signals, and
- calculating the tag position \mathbf{p} using estimated $(d_{\mathbf{B}}^{(i,j)}, \theta_2^{(j)}, \phi_2^{(j)})$ from all TXs and RXs.

To simplify the notations, we avoid superscript i, j when the indices of the TX and RX are clear from the context.

B. Signal Model

In the following, we describe a bistatic signal model for an arbitrary i -th TX and j -th RX. Note that, collectively, the set of all TXs and RXs constitutes a multistatic system, where each individual pair of TX, RX is a bistatic system.

We consider the receivers are equipped uniformly-spaced N_{a} -element antenna array. Denoting the position of i -th

element of the antenna array by $[x_i, y_i, z_i]^{\top}$, we define the $(N_{\text{a}} \times 1)$ array response vector of the RX as

$$\begin{aligned} \mathbf{a}(\theta, \phi) = & \left[\exp \left(j \frac{2\pi}{\lambda} ((x_i - x_0) \cos \theta \sin \phi \right. \right. \\ & \left. \left. + (y_i - y_0) \sin \theta \sin \phi + (z_i - z_0) \cos \phi) \right) \right]_{i=0}^{N_{\text{a}}-1}. \end{aligned} \quad (3)$$

We consider the TXs transmit an OFDM-based wideband illumination signal, also called the carrier signal, with the center frequency F_c and N_s equally-spaced subcarriers spanning the bandwidth B . The tag reflects the illumination signal by shifting the center frequency to $F_c + F_{\text{shift}}$, and modulating a packet on it. We call this reflected signal the backscatter signal. In the following, we model the channels experienced by the carrier and the backscatter channels.

1) Carrier Channel: We consider L_0 propagation paths between the TX and RX, and denote the complex-valued coefficient, the bandwidth-normalized delay¹ and azimuth/elevation angles of ℓ -th propagation path by $\alpha_{0,\ell}, \tau_{0,\ell}, \theta_{0,\ell}, \phi_{0,\ell}$, respectively. We extend the single-antenna channel model from [10] to write the channel frequency response (CFR) of the TX-RX channel, called carrier channel, for multi-antenna RX as

$$\begin{aligned} \mathcal{H}_{0,n} = & \sum_{\ell=0}^{L_0-1} \alpha_{0,\ell} \exp \left[-j 2\pi \left(\frac{F_c}{B} + \frac{n}{N_s} \right) \tau_{0,\ell} \right] \mathbf{a}^{\top}(\theta_{0,\ell}, \phi_{0,\ell}), \end{aligned} \quad (4)$$

where n denotes the subcarrier index.

After down-conversion to baseband and concatenating $\mathcal{H}_{0,n}$ for all subcarriers, we have $\mathcal{H}_0 = [\mathcal{H}_{0,-N_s/2}^{\top}, \dots, \mathcal{H}_{0,N_s/2-1}^{\top}]^{\top} \in \mathbb{C}^{N_s \times N_{\text{a}}}$. Then, \mathcal{H}_0 satisfies the factorization

$$\mathcal{H}_0 = \mathbf{F}(\tau_0) \mathbf{D}_0 \mathbf{A}^{\top}(\theta_0, \phi_0), \quad (5)$$

where

$$\mathbf{F}(\tau) = [\mathbf{f}(\tau_{0,0}, \dots, \mathbf{f}(\tau_{0,L-1})] \in \mathbb{C}^{N_s \times L}, \quad (6)$$

$$\mathbf{f}(\tau) = \left[e^{j \frac{2\pi(N_s/2)}{N_s} \tau}, \dots, e^{j \frac{-2\pi(N_s/2-1)}{N_s} \tau} \right] \in \mathbb{C}^{N_s \times 1}, \quad (7)$$

$$\mathbf{D}_0 = \text{Diag}(\alpha_{0,0}, \dots, \alpha_{0,L-1}) \in \mathbb{C}^{L \times L}, \quad (8)$$

$$\mathbf{A}(\theta_0, \phi_0) = [\mathbf{a}(\theta_{0,0}, \phi_{0,0}), \dots, \mathbf{a}(\theta_{0,L-1}, \phi_{0,L-1})] \in \mathbb{C}^{N_{\text{a}} \times L}. \quad (9)$$

2) Backscatter Channel: Similarly, we consider L_1 propagation paths between the TX and the tag, and denote the complex-valued coefficient, the bandwidth-normalized delay and AoA of ℓ -th path by $\alpha_{1,\ell}, \tau_{1,\ell}, \theta_{1,\ell}, \phi_{1,\ell}$, respectively. Then, the TX-Tag CFR is

$$\mathcal{H}_{1,n} = \sum_{\ell=0}^{L_1-1} \alpha_{1,\ell} \exp \left[-j 2\pi \left(\frac{F_c}{B} + \frac{n}{N_s} \right) \tau_{1,\ell} \right], \quad (10)$$

where n is the subcarrier index.

¹If the delay is t , then the normalized delay is $\tau = Bt$ assuming the sampling rate of B . In practice, the RX sampling rate is higher than the bandwidth B . For the range and angle estimation, however, the sampling rate any more than the bandwidth does not provide further benefit. Hence, we assume the sampling rate of B .

Similarly, we consider L_2 propagation paths between the tag and the RX, and denote the complex-valued coefficient, the bandwidth-normalized delay and AoA of ℓ -th path by $\alpha_{2,\ell}, \tau_{2,\ell}, \theta_{2,\ell}, \phi_{2,\ell}$, respectively. Furthermore, the tag shifts the illumination signal by F_{shift} . Therefore, the Tag-RX CFR can be defined as

$$\mathcal{H}_{2,n} = \sum_{\ell=0}^{L_2-1} \alpha_{2,\ell} \exp \left[-j2\pi \left(\frac{F_c + F_{\text{shift}}}{B} + \frac{n}{N_s} \right) \tau_{2,\ell} \right] \mathbf{a}^\top (\theta_{2,\ell}, \phi_{2,\ell}) \quad (11)$$

$$= \sum_{\ell=0}^{L_1-1} \sum_{m=0}^{L_2-1} \left[\alpha_{1,\ell} \alpha_{2,m} \exp \left(-j \frac{2\pi n}{N_s} (\tau_{1,\ell} + \tau_{2,m}) \right) \right. \\ \left. \exp \left(-j2\pi \left(\frac{F_{\text{shift}}}{B} \right) \tau_{2,m} \right) \mathbf{a}^\top (\theta_{2,m}, \phi_{2,m}) \right]. \quad (13)$$

Let a bistatic path, indexed by $\ell' = \ell + L_1 m$, denote the total signal path over ℓ -th path in the TX-Tag channel and m -th path in the Tag-RX channel. Then, the effective channel coefficient, the normalized delay, and the AoA of ℓ' -th bistatic path can be given by $\beta_{\ell'} = \alpha_{1,\ell} \alpha_{2,m} e^{-j2\pi F_{\text{shift}} \tau_{2,m}/B}$, $\tau_{\mathbf{B},\ell'} = \tau_{1,\ell} + \tau_{2,m}$, and $\theta_{\mathbf{B},\ell'} = \theta_{2,m}, \phi_{\mathbf{B},\ell'} = \phi_{2,m}$. As a result, (13) can be simplified to

$$\mathcal{H}_{\mathbf{B},n} = \sum_{\ell=0}^{L_1 L_2 - 1} \beta_\ell \exp \left(-j \frac{2\pi n}{N_s} \tau_{\mathbf{B},\ell} \right) \mathbf{a}^\top (\theta_{\mathbf{B},\ell}, \phi_{\mathbf{B},\ell}). \quad (14)$$

Concatenating $\mathcal{H}_{\mathbf{B},n}$ for all subcarriers, we have $\mathcal{H}_{\mathbf{B}} = [\mathcal{H}_{\mathbf{B},-N_s/2}^\top, \dots, \mathcal{H}_{\mathbf{B},N_s/2-1}^\top]^\top \in \mathbb{C}^{N_s \times N_a}$. We define $L = L_1 L_2$ as the total number of bistatic paths in the backscatter channel. Then, $\mathcal{H}_{\mathbf{B}}$ satisfies the factorization

$$\mathcal{H}_{\mathbf{B}} = \mathbf{F}(\tau_{\mathbf{B}}) \mathbf{D}_{\mathbf{B}} \mathbf{A}^\top (\theta_{\mathbf{B}}, \phi_{\mathbf{B}}), \quad (15)$$

where, $\mathbf{D}_{\mathbf{B}} = \text{Diag}(\beta_0, \dots, \beta_{L-1}) \in \mathbb{C}^{L \times L}$.

In practice, the RX does not have access to the channel information directly, but processes the received signal to get the channel estimates [10]. We denote an estimate of the channel \mathcal{H} by $\hat{\mathcal{H}}$. Furthermore, the RX processes N_{sym} OFDM symbols to get a channel estimate. Let $\hat{\mathcal{H}}[k]$ denote the estimate of \mathcal{H} using k -th OFDM symbol. Therefore, the RX has access to $\hat{\mathcal{H}}_0[k], \hat{\mathcal{H}}_{\mathbf{B}}[k], \forall k \in \{1, \dots, N_{\text{sym}}\}$ to estimate $\tau_{\mathbf{B},0}, \theta_{\mathbf{B},0}$ and $\phi_{\mathbf{B},0}$. We assume the channels remain static for the duration of N_{sym} symbols.

In next section, we discuss the joint range-angle estimation algorithms using these channel estimates. Without loss of generality, we subsequently assume the first path in all channels are the LoS path of the channels. Therefore, $\tau_i = \tau_{i,0}, \theta_i = \theta_{i,0}, \phi_i = \phi_{i,0}, i \in \{0, 1, 2, \mathbf{B}\}$. Furthermore, $\tau_i = Bd_i/c$.

III. Joint Bistatic Range and angle Estimation

For tag localization, we are interested in estimating the parameters $(\tau_{\mathbf{B},0}, \theta_{\mathbf{B},0}, \phi_{\mathbf{B},0})$ of the LoS path in the backscatter channel corresponding to an arbitrary TX-RX pair.

Notably, the bistatic range (or delay $\tau_{\mathbf{B},0}$) estimation uses time difference of arrival (TDoA) method with the arrival of carrier signal as the reference [10]. This key design feature enables the ranging without requiring a separate clock sharing infrastructure between TXs and RXs in the network. Accordingly, let the TDoA estimate between the signal over the backscatter channel $\mathcal{H}_{\mathbf{B}}$ and the signal over the carrier channel \mathcal{H}_0 be denoted by $\Delta\hat{\tau}$. Then, given the known TX-RX distance d_0 , the estimate of the bistatic range is

$$\hat{d}_B = \frac{c}{B} (\Delta\hat{\tau} + \tau_{0,0}). \quad (16)$$

Estimating the TDoA $\Delta\hat{\tau}$ involves estimating the time of arrival (ToA) over the backscatter channel $\mathcal{H}_{\mathbf{B}}$ and the carrier channel \mathcal{H}_0 . Each ToA can be estimated using the channel impulse response (CIR)-based method as investigated in Section III.C of [10].

In this work, in addition to estimating the bistatic range, we also estimate the AoA of the LoS path in the backscatter channel. This requires two ToA estimates, one from the carrier and one from the backscatter channel, and one AoA estimate from the backscatter channel. To achieve this, we consider two approaches: (i) joint estimation of range and angle, and (ii) stage-wise estimation. The joint approach is employed by the baseline algorithms 2D-FFT and 2D-MUSIC described in Section III-A and III-B, as well as the proposed algorithm JRAC in Section III-D. The stage-wise approach is used in the proposed algorithm SRAE in Section III-C.

For the purposes of this work, we consider a ULA at the RXs and thus, estimate only azimuthal angles. Therefore, in this section, we assume $\phi_{\mathbf{B},0} = \pi/2$. However, the proposed methods can be extended to enable estimating $\phi_{\mathbf{B},0}$ with minimal modifications.

Finally, we define the delay and angle grid as the ordered sets

$$\mathcal{T} = \left\{ \frac{N_s i}{G_\tau} \middle| i = 0, \dots, G_\tau - 1 \right\} \quad \text{and} \quad (17)$$

$$\Theta = \left\{ \sin^{-1} \left(\frac{2j}{G_\theta} \right) \middle| j = -G_\theta/2, \dots, G_\theta/2 - 1 \right\}, \quad (18)$$

respectively, such that $|\mathcal{T}| = G_\tau$ and $|\Theta| = G_\theta$.

A. 2D FFT

Let the 2D spectrum of $\hat{\mathcal{H}}_i$ be

$$S_i^{\text{2DFFT}}(\tau, \theta) = \sum_{k=1}^{N_{\text{sym}}} \left| \sum_{m=-N_s/2}^{N_s/2-1} \sum_{n=0}^{N_a-1} [\hat{\mathcal{H}}_i[k]]_{m+N_s/2+1, n+1} e^{j2\pi \left(\frac{\tau m}{N_s} + \frac{v n}{2} \right)} \right|, \quad (19)$$

where, $\tau \in \mathcal{T}$, $v = \sin \theta$ for $\theta \in \Theta$, and $i \in \{0, \mathbf{B}\}$. We define the set of (τ, θ) where $|S_i^{\text{2DFFT}}|$ has a peak above a threshold T_{\min}^{2DFFT} as

$$\mathcal{P}_i^{\text{2DFFT}} = \left\{ (\tau_j, \theta_\ell) \in \mathcal{T} \times \Theta \middle| |S_i^{\text{2DFFT}}(\tau_j, \theta_\ell)| > T_{\min}^{\text{2DFFT}}, \right. \\ |S_i^{\text{2DFFT}}(\tau_j, \theta_{\ell-1})| < |S_i^{\text{2DFFT}}(\tau_j, \theta_\ell)| > |S_i^{\text{2DFFT}}(\tau_j, \theta_{\ell+1})|, \\ \left. |S_i^{\text{2DFFT}}(\tau_{j-1}, \theta_\ell)| < |S_i^{\text{2DFFT}}(\tau_j, \theta_\ell)| > |S_i^{\text{2DFFT}}(\tau_{j+1}, \theta_\ell)| \right\}. \quad (20)$$

We then estimate the ToA of the carrier signal $\hat{\tau}_{0,0}$ from $\mathcal{P}_0^{\text{2DFFT}}$ as

$$\hat{\tau}_{0,0} = \arg \min_{\tau: (\tau, \theta) \in \mathcal{P}_0^{\text{2DFFT}}} \tau. \quad (21)$$

Subsequently, we estimate the ToA and the AoA of the backscatter signal $(\hat{\tau}_{\mathcal{B},0}, \hat{\theta}_{\mathcal{B},0})$ from $\mathcal{P}_{\mathcal{B}}^{\text{2DFFT}}$ as

$$\begin{aligned} \hat{\tau}_{\mathcal{B},0} &= \min_{\substack{(\tau, \theta) \in \mathcal{P}_{\mathcal{B}}^{\text{2DFFT}} \\ \tau > \hat{\tau}_{0,0}}} \tau, \\ \hat{\theta}_{\mathcal{B},0} &= \arg \max_{\theta: (\hat{\tau}_{\mathcal{B},0}, \theta) \in \mathcal{P}_{\mathcal{B}}^{\text{2DFFT}}} |S_{\mathcal{B}}^{\text{2DFFT}}(\hat{\tau}_{\mathcal{B},0}, \theta)|. \end{aligned} \quad (22)$$

We use the resultant triplet $(\hat{\tau}_{0,0}, \hat{\tau}_{\mathcal{B},0}, \hat{\theta}_{\mathcal{B},0})$ to estimate the bistatic range and the AoA as follows:

$$\hat{d}_{\mathcal{B}} = \frac{c}{B}(\tau_{0,0} + \hat{\tau}_{\mathcal{B},0} - \hat{\tau}_{0,0}), \quad \text{and} \quad \hat{\theta}_{\mathcal{B}} = \hat{\theta}_{\mathcal{B},0}. \quad (23)$$

Finally, $(\hat{d}_{\mathcal{B}}, \hat{\theta}_{\mathcal{B}})$ presents the resultant range-angle pair associated to the TX-Tag-RX path. The computational complexity of the 2D FFT method is $\mathcal{O}(G_{\tau}G_{\theta} \log_2(G_{\tau}G_{\theta}))$.

B. 2D MUSIC

Two-dimensional MUSIC algorithm is an extension of MUSIC algorithm to jointly estimate ToA and AoA [25], [29]. We use this algorithm to estimate $(\hat{d}_{\mathcal{B}}, \hat{\theta}_{\mathcal{B}})$ for a bistatic system.

Let the measurement vector $\hat{\mathbf{h}}_i[k] = \text{vec}(\hat{\mathcal{H}}_i[k]) \in \mathbb{C}^{N_s N_a \times 1}$ be a stack of the channel estimates of all the subcarriers at all the antennas, for $i = \{0, \mathcal{B}\}$ and $k = \{1, \dots, N_{\text{sym}}\}$. Then, from (5) and (15), we have

$$\hat{\mathbf{h}}_i[k] = \text{vec}(\mathcal{H}_i[k]) + \mathbf{v}_i[k] \quad (24)$$

$$\stackrel{(a)}{=} \text{vec}(\mathbf{F}(\boldsymbol{\tau}_i) \mathbf{D}_i \mathbf{A}^{\top}(\boldsymbol{\theta}_i)) + \mathbf{v}_i[k] = \mathbf{U}(\boldsymbol{\tau}_i, \boldsymbol{\theta}_i) \boldsymbol{\gamma}_i[k] + \mathbf{v}_i[k],$$

where $\mathbf{v}_i[k]$ denotes channel estimation error, (a) assumes static channel over N_{sym} symbols, $\boldsymbol{\gamma}_0 = \boldsymbol{\alpha}_0$, $\boldsymbol{\gamma}_{\mathcal{B}} = \boldsymbol{\beta}_{\mathcal{B}}$, and

$$\mathbf{U}(\boldsymbol{\tau}, \boldsymbol{\theta}) = [\mathbf{a}(\theta_0) \otimes \mathbf{f}(\tau_0), \dots, \mathbf{a}(\theta_{L-1}) \otimes \mathbf{f}(\tau_{L-1})]. \quad (25)$$

The collected observations from all N_{sym} OFDM symbols is given by

$$\mathbf{Y}_i = [\hat{\mathbf{h}}_i[1], \dots, \hat{\mathbf{h}}_i[N_{\text{sym}}]] = \mathbf{U}(\boldsymbol{\tau}_i, \boldsymbol{\theta}_i) (\boldsymbol{\gamma}_i \otimes \mathbf{1}_{N_{\text{sym}}}^{\top}) + \mathbf{V}_i, \quad (26)$$

where $\mathbf{V}_i = [\mathbf{v}_i[1], \dots, \mathbf{v}_i[N_{\text{sym}}]] \in \mathbb{C}^{N_s N_a \times N_{\text{sym}}}$.

The 2D MUSIC algorithm is based on decomposition of the sample covariance matrix, $\mathbf{R}_{\mathbf{Y}_i} = \frac{1}{N_{\text{sym}}} \mathbf{Y}_i \mathbf{Y}_i^H$, into the signal subspace \mathbf{E}_S and noise subspace \mathbf{E}_N as

$$\mathbf{R}_{\mathbf{Y}_i} = \mathbf{E}_{S,i} \boldsymbol{\Lambda}_{S,i} \mathbf{E}_{S,i}^H + \mathbf{E}_{N,i} \boldsymbol{\Lambda}_{N,i} \mathbf{E}_{N,i}^H, \quad (27)$$

where $\boldsymbol{\Lambda}_{S,i}$ and $\boldsymbol{\Lambda}_{N,i}$ are diagonal matrices with the eigenvalues of the corresponding subspaces. Assuming the number of signal space K_i , $\boldsymbol{\Lambda}_{S,i}$ and $\mathbf{E}_{S,i}$ are determined by using the K_i -largest eigenvalues and associated eigenvectors of $\mathbf{R}_{\mathbf{Y}_i}$, whereas $\boldsymbol{\Lambda}_{N,i}$ and $\mathbf{E}_{N,i}$ are determined using the remaining $N_s N_a - K_i$ eigenvalues and the associated eigenvectors. In practice, the value of K_i 's is typically unknown and various criterion such as Minimum Description Length (MDL), Akaike Information Criterion (AIC) are used for estimating K_i 's.

The orthogonality between $\mathbf{u}(\tau, \theta) = \mathbf{a}(\theta) \otimes \mathbf{f}(\tau)$ and the noise subspace is measured as $\|\mathbf{u}(\tau, \theta)^H \mathbf{E}_N\|_2^2$, and its inverse forms the pseudo-spectrum of 2D MUSIC as

$$S_i^{\text{2DMUSIC}}(\tau, \theta) = (\mathbf{u}(\tau, \theta)^H \mathbf{E}_{N,i} \mathbf{E}_{N,i}^H \mathbf{u}(\tau, \theta))^{-1}, \quad (28)$$

for $(\tau, \theta) \in \mathcal{T} \times \Theta$ and $i \in \{0, \mathcal{B}\}$.

Finally, to estimate $(\hat{d}_{\mathcal{B}}, \hat{\theta}_{\mathcal{B}})$ from S_i^{2DMUSIC} , $i \in \{0, \mathcal{B}\}$, the procedure described in (20)-(23) is followed, albeit with the quantities $T_{\min}^{\text{2DMUSIC}}$ and $\mathcal{P}_i^{\text{2DMUSIC}}$.

The computational complexity of the 2D-MUSIC algorithm is dominated by three main components. First, the eigenvalue decomposition (EVD) of the sample covariance matrix $\mathbf{R}_{\mathbf{Y}_i}$ incurs a cost of $\mathcal{O}(N_a^3 N_s^3)$. Second, the matrix multiplication in (28) involving matrices of size $N_a N_s \times 1$ and $N_a N_s \times (N_a N_s - K_i)$ contributes to the complexity of $\mathcal{O}(N_a^2 N_s^2)$. Finally, the pseudo-spectrum calculation, which evaluates the spectrum over $G_{\tau} G_{\theta}$ grid points, scales the computational complexity linearly with the number of grid points. Therefore, the computational complexity of the 2D MUSIC algorithm is $\mathcal{O}(G_{\tau} G_{\theta} N_a^2 N_s^2 + N_a^3 N_s^3)$. This computational cost may pose significant limitations for practical implementations. Therefore, in the following sections, we investigate alternative approaches for joint range and angle estimation that offer improved computational efficiency.

C. Stage-wise Range-Angle Estimation (SRAE)

This algorithm operates in two stages:

1) Stage 1 (Delay estimation): To estimate the LoS delay $\hat{\tau}_i$, we apply the (one-dimensional) MUSIC algorithm in the delay domain. The sample covariance matrix is defined as

$$\mathbf{R}_{\hat{\mathcal{H}}_i} = \frac{1}{N_{\text{sym}}} \sum_{k=1}^{N_{\text{sym}}} \hat{\mathcal{H}}_i[k] \hat{\mathcal{H}}_i^H[k] \in \mathbb{C}^{N_s \times N_s}. \quad (29)$$

The covariance matrix is then decomposed into the signal subspace \mathbf{E}_S and noise subspace \mathbf{E}_N using the MDL criterion. The MUSIC spectrum is then calculated as

$$S_i^{\text{SRAE}}(\tau) = (\mathbf{f}(\tau)^H \mathbf{E}_{N,i} \mathbf{E}_{N,i}^H \mathbf{f}(\tau))^{-1}. \quad (30)$$

Then, the peak search is performed on the delay-spectrums of the carrier and backscatter channels, such that

$$\begin{aligned} \hat{\tau}_{0,0} &= \min \left\{ \tau_j \in \mathcal{T} \mid S_0^{\text{SRAE}}(\tau_j) > T_{\min}^{\text{SRAE}}, \right. \\ &\quad \left. S_0^{\text{SRAE}}(\tau_{j-1}) < S_0^{\text{SRAE}}(\tau_j) > S_0^{\text{SRAE}}(\tau_{j+1}) \right\}, \end{aligned} \quad (31)$$

$$\begin{aligned} \hat{\tau}_{\mathcal{B},0} &= \min \left\{ \tau_j \in \mathcal{T} \mid \tau_j > \hat{\tau}_{0,0}, S_{\mathcal{B}}^{\text{SRAE}}(\tau_j) > T_{\min}^{\text{SRAE}}, \right. \\ &\quad \left. S_{\mathcal{B}}^{\text{SRAE}}(\tau_{j-1}) < S_{\mathcal{B}}^{\text{SRAE}}(\tau_j) > S_{\mathcal{B}}^{\text{SRAE}}(\tau_{j+1}) \right\}. \end{aligned} \quad (32)$$

Using the delay estimates $\hat{\tau}_{0,0}, \hat{\tau}_{\mathcal{B},0}$, the bistatic range estimate can be determined using (23).

2) Stage 2 (AoA estimation): The complex gains of the channel taps associated to the LoS path for all antennas can be retrieved using the channel estimate $\hat{\mathcal{H}}_{\mathcal{B}}$. These taps associated to the delay $\hat{\tau}_{\mathcal{B},0}$ is given by

$$\hat{\mathbf{x}}_{\mathcal{B}}[k] = \mathbf{f}(\hat{\tau}_{\mathcal{B},0})^{\dagger} \hat{\mathcal{H}}_{\mathcal{B}}[k], \quad k \in \{1, \dots, N_{\text{sym}}\}, \quad (33)$$

The AoA estimation of the LoS path of the backscatter channel, $\hat{\theta}_{\mathcal{B}}$, is obtained based on the relative phases of $\hat{\mathbf{x}}_{\mathcal{B}}$, again by applying either beamforming or subspace-based methods. In this instance, we run another round of MUSIC in a spatial domain. The relevant sample covariance $\mathbf{R}_{\mathbf{x}_{\mathcal{B}}} = \frac{1}{N_{\text{sym}}} \sum_{k=1}^{N_{\text{sym}}} \mathbf{x}_{\mathcal{B}}[k] \mathbf{x}_{\mathcal{B}}[k]^H$, is decomposed into the

signal subspace $\mathbf{E}_{S,B}$ and noise subspace denoted by $\mathbf{E}_{N,B}$. Note that, given there is only single-delay (and hence, single path) in (33), the size of the signal subspace is 1. The orthogonality between $\mathbf{a}(\theta)$ and the noise subspace is measured as $\|\mathbf{a}(\theta)^H \mathbf{E}_N\|_2^2$, the inverse of which forms the MUSIC spectrum in spatial domain. This spectrum is searched for the peaks as

$$\hat{\theta}_B = \operatorname{argmax}_{\theta \in \Theta} \frac{1}{\mathbf{a}(\theta)^H \mathbf{E}_{N,B} \mathbf{E}_{N,B}^H \mathbf{a}(\theta)}. \quad (34)$$

SRAE method is equivalent to applying two one-dimensional MUSIC algorithms. The computational complexity of range estimation is $\mathcal{O}(G_\tau N_s^3)$, while the complexity of the AoA estimation is $\mathcal{O}(G_\theta N_a^3)$. Therefore, the overall computational complexity is $\mathcal{O}(G_\tau N_s^3 + G_\theta N_a^3)$.

With the SRAE algorithm, the accuracy of delay estimation affects the accuracy of the estimated taps, and consequently, of the AoA estimation. Hence, this stage-wise approach remains sub-optimal, in fact, irrespective of the order of estimating the parameters. Thus, we next introduce a joint estimation method based on clustering on the joint range-angle heatmap.

D. Joint Range-Angle Clustering (JRAC)

The JRAC method follows a four-step process: First, similar to SRAE, it identifies the appropriate search space in delay domain. Second, it estimates a 2D heatmap for the estimated delay space and the entire spatial domain. Third, it clusters various channel taps. Finally, it selects the cluster with the lowest delay to retrieve the delay and angle corresponding to the LoS path. In the following, we formally describe each of these steps in detail. The outline of our algorithm is given in Algorithm 1.

1) Step 1 (Truncate the search space in delay-domain): We first truncate the possible delay space using 1D MUSIC in the delay domain. Specifically, we use S_i^{SRAE} , $i \in \{0, B\}$ from (30), and the threshold T_{\min}^{JRAC} to determine the truncated delay space as

$$\mathcal{T}_i = \{\tau \in \mathcal{T} | S_i^{\text{SRAE}}(\tau) \geq T_{\min}^{\text{JRAC}}\}, i \in \{0, B\}. \quad (35)$$

2) Step 2 (The range-angle heatmaps and clipping): We define the 2D heatmap associated to the estimated channels $\hat{\mathcal{H}}_i$ as

$$S_i^{\text{JRAC}}(\tau, \theta) = \sum_{k=1}^{N_{\text{sym}}} \left\| \mathbf{f}(\tau)^H \hat{\mathcal{H}}_i[k] \mathbf{a}^*(\theta) \right\|^2, \quad \tau \in \mathcal{T}_i, \theta \in \Theta, \quad i \in \{0, B\}. \quad (36)$$

Note that, this heatmap is similar to the oversampled 2D FFT spectrum described in (19), albeit with a truncated delay space with reduced computational cost. Hence, it is possible to estimate the bistatic range and angle using equations (20)-(23). However, in the following, we introduce a clustering step which can provide a robust estimate in an heavily multipath environment.

Let T_{\max}^{JRAC} denote a lower clipping threshold and $s_{\max,i} = \max_{\tau \in \mathcal{T}_i, \theta \in \Theta} S_i^{\text{JRAC}}(\tau, \theta)$ denote the maximum value of the heatmaps for $i \in \{0, B\}$. We define a clipped normalized spectrum as

$$\bar{S}_i^{\text{JRAC}}(\tau, \theta) = S_i^{\text{JRAC}}(\tau, \theta) \mathbf{1}\{S_i^{\text{JRAC}}(\tau, \theta) \geq T_{\max}^{\text{JRAC}} s_{\max,i}\}. \quad (37)$$

Notably, \bar{S}_i^{JRAC} , $i \in \{0, B\}$ have islands of clusters.

Algorithm 1 Joint Range-Angle Clustering (JRAC)

Input $\hat{\mathcal{H}}_i[k], \tau_{0,0}, \mathcal{T}, \Theta$, Thresholds T_{\min}^{JRAC} and T_{\max}^{JRAC} .

- 1: for $i \in \{0, B\}$ do
 - Step 1: Truncate the search space in delay-domain
 - 2: Calculate $S_0^{\text{SRAE}}(\tau)$ and $S_B^{\text{SRAE}}(\tau)$ according to (30).
 - 3: Truncate the delay search space \mathcal{T} to get $\mathcal{T}_0, \mathcal{T}_B$ as

$$\mathcal{T}_0 = \left\{ \tau \in \mathcal{T} \mid S_0^{\text{SRAE}}(\tau) \geq T_{\min} \right\},$$

$$\mathcal{T}_B = \left\{ \tau \in \mathcal{T} \mid S_B^{\text{SRAE}}(\tau) \geq T_{\min} \right\}.$$
 - Step 2: The range-angle heatmaps and clipping
 - 4: Get the 2D heatmap $S_i^{\text{JRAC}}(\tau, \theta), \forall \tau \in \mathcal{T}_i, \theta \in \Theta$ using (36).
 - 5: Find the maxima of the heatmap $s_{\max,i} = \max_{\tau, \theta} S_i^{\text{JRAC}}(\tau, \theta)$, then clip the S_i^{JRAC} such that

$$\bar{S}_i^{\text{JRAC}}(\tau, \theta) = S_i^{\text{JRAC}}(\tau, \theta) \mathbf{1}\{S_i^{\text{JRAC}}(\tau, \theta) \geq T_{\max}^{\text{JRAC}} s_{\max,i}\}.$$
 - Step 3.a: Clustering in delay-domain
 - 6: Calculate $\bar{s}_i(\tau) = \sum_{\ell=1}^{|\Theta|} \bar{S}_i^{\text{JRAC}}(\tau, \theta_\ell), \forall \tau \in \mathcal{T}_i$.
 - 7: Determine boundaries of the delay-domain clusters by

$$t_{i,j} = \begin{cases} 0, j = 0 \text{ or } j = |\mathcal{T}_i| + 1, \\ 1, \bar{s}_i(\tau_j) \neq 0, \\ 0, \bar{s}_i(\tau_j) = 0, \end{cases} \quad j \in \{0, \dots, |\mathcal{T}_i| + 1\},$$
 - 8: $b_{i,j} = t_{i,j+1} - t_{i,j}, j \in \{0, \dots, |\mathcal{T}_i|\}$.
 - 9: Determine the range-clusters $\mathcal{D}_{i,m}$ using (40).
 - Step 3.b: Clustering in angle-domain
 - 10: Calculate $\bar{s}_i(\theta_\ell) = \sum_{j=1}^{|\mathcal{T}_i|} \bar{s}_i(\tau_j, \theta_\ell), \forall \theta_\ell \in \Theta$.
 - 11: Repeat Steps 7-9 to detect the angle-clusters. Denote n -th cluster as $\mathcal{A}_{i,n}$.
 - Step 4: Estimation
 - 12: Let k -th cluster $\mathcal{C}_{i,k} = \mathcal{D}_{i,m} \times \mathcal{A}_{i,n}$.
 - 13: Determine the local maxima within each cluster as

$$(\hat{\tau}_{i,k}, \hat{\theta}_{i,k}) = \arg \max_{(j, \ell) \in \mathcal{C}_{i,k}} \bar{S}_i^{\text{JRAC}}(\tau_j, \theta_\ell).$$
 - 14: Find the LoS cluster indexed by $k_i^* = \arg \min_k \hat{\tau}_{i,k}$.
 - 15: end for
 - 16: Calculate $\hat{\tau}_{0,0} = \tau_{0,k_0^*}, \hat{\tau}_{B,0} = \tau_{B,k_B^*}, \hat{\theta}_{B,0} = \theta_{B,k_B^*}$.
 - 17: Repeat steps 4-9 on $S_0^{\text{JRAC}}(\theta, \tau)$ to estimate the TX-RX delay $\hat{\tau}_{0,0}$.
 - 18: Calculate the LoS bistatic range and angle as

$$\hat{d}_B = \frac{c}{B} (\tau_{0,0} + \hat{\tau}_{B,0} - \hat{\tau}_{0,0}) \quad \text{and} \quad \hat{\theta}_B = \hat{\theta}_{B,0}.$$
 - Output The estimated bistatic range and angle as $(\hat{d}_B, \hat{\theta}_B)$.

3) Step 3 (Clustering): We now identify the boundaries of the clusters in the delay and angle domain.

a) Delay Domain: For $i \in \{0, B\}$, let $\bar{s}_i(\tau)$ denote the angle-wise aggregated $\bar{S}_i^{\text{JRAC}}(\tau, \theta)$, such that

$$\bar{s}_i(\tau) = \sum_{\ell=1}^{|\Theta|} \bar{S}_i^{\text{JRAC}}(\tau, \theta_\ell), \quad \forall \tau \in \mathcal{T}_i, i \in \{0, B\}. \quad (38)$$

We then determine the non-zero points $t_{i,j}$ of the range-clusters and the boundary indicators $b_{i,j}$ in the delay domain as

$$t_{i,j} = \begin{cases} 0, j = 0 \text{ or } j = |\mathcal{T}_i| + 1, \\ 1, \bar{s}_i(\tau_j) \neq 0, \\ 0, \bar{s}_i(\tau_j) = 0, \end{cases} \quad j \in \{0, \dots, |\mathcal{T}_i| + 1\},$$

$$b_{i,j} = t_{i,j+1} - t_{i,j}, \quad j \in \{0, \dots, |\mathcal{T}_i|\}. \quad (39)$$

Note that for every $b_{i,\alpha} = 1$, there is an associated $\beta > \alpha$, such that $b_{i,\beta} = -1$ and $b_{i,j''} = 0, \forall \alpha < j'' < \beta$. This

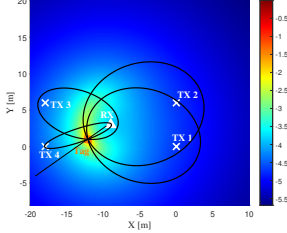


Fig. 2. Elliptical positioning scenario with bistatic range measurements from four TXs and one RX. The tag's location is determined as the intersection of the four ellipses, each defined by a TX–RX pair as its foci and the hyperplane from the estimated tag AoA.

indicates the existence of a start and end boundaries of all delay-clusters.

Let \mathbf{D}_i define the set of the tuples (α_m, β_m) containing the index of the start boundary α_m and the end boundary β_m of m -th delay-cluster. We define m -th delay-cluster as

$$\mathcal{D}_{i,m} = \{j'' | \alpha_m < j'' < \beta_m, \exists (\alpha_m, \beta_m) \in \mathbf{D}_i\}. \quad (40)$$

Note that, $\cup_m \mathcal{D}_{i,m} = \{j | t_{i,j} = 1\}$ represents all indices j with non-zero values at $\bar{s}_i(\tau_j)$.

b) Angle Domain: Similarly, we denote the delay-wise aggregated $\bar{s}_i(\tau, \theta)$ by $\bar{s}_i(\theta)$, and determine the n -th angle-cluster $\mathcal{A}_{i,n}$ using (38)-(40).

4) Step 4 - Estimation: Let the k -th cluster in the heatmap be defined using the m -th delay-cluster and n -th angle cluster as $\mathcal{C}_{i,k} = \mathcal{D}_{i,m} \times \mathcal{A}_{i,n}$. The algorithm searches for the local maxima within each cluster as

$$(\hat{\tau}_{i,k}, \hat{\theta}_{i,k}) = \arg \max_{(j, \ell) \in \mathcal{C}_{i,k}} \bar{s}_i^{\text{JRAC}}(\tau_j, \theta_\ell). \quad (41)$$

Then, the cluster associated to the LoS path corresponds to the one with minimum delay. Therefore,

$$k^* = \arg \min_k \hat{\tau}_{i,k}, \quad (42)$$

$$\hat{\tau}_{0,0} = \tau_{0,k^*}, \hat{\theta}_{\text{B},0} = \theta_{\text{B},k^*}, \hat{\theta}_{\text{B},0} = \theta_{\text{B},k^*}. \quad (43)$$

Finally, following (23),

$$\hat{d}_{\text{B}} = \frac{c}{B}(\tau_{0,0} + \hat{\theta}_{\text{B},0} - \hat{\tau}_{0,0}), \quad \text{and} \quad \hat{\theta}_{\text{B}} = \hat{\theta}_{\text{B},0}, \quad (44)$$

we get $(\hat{d}_{\text{B}}, \hat{\theta}_{\text{B}})$, the resultant bistatic range-angle pair associated to the backscatter path.

The computational complexity of the JRAC algorithm is dominated by two steps: First, the MUSIC algorithm used in Step 1 for truncating the delay domain has complexity $\mathcal{O}(G_\tau N_s^3)$. Second, the computation of determining the heat map in (36) has complexity $\mathcal{O}(G_\tau G_\theta N_s N_a)$. The Step 3 and 4 are one-dimensional searches with the complexity $\mathcal{O}(G_\tau + G_\theta)$. Therefore, the overall computational complexity of the JRAC algorithm is $\mathcal{O}(G_\tau N_s^3 + G_\tau G_\theta N_s N_a)$.

IV. Positioning

In this section, we propose two real-time multi-static positioning algorithms. As shown in Fig. 2, the multi-static positioning scenario with range-angle measurements reduces to finding the intersection of the ellipses, each defined by a TX–RX pair as its foci, along with the hyperplane determined by the estimated tag AoA. In the most general scenario, only a subset of receivers are equipped with antenna arrays that enable AoA estimation.

Therefore, our subsequent formulation allows for range and angle measurements from different receivers to be exploited separately and does not assume that both range-angle estimates come from the same receiver.

Let \hat{d}_n denote the bistatic range estimate of n -th measurement from the i_n -th TX and j_n -th RX. Denoting the noise in the range measurements as $\eta_{r,n}$, we can write

$$\hat{d}_n = \|\mathbf{p} - \mathbf{p}_{\text{TX},i_n}\| + \|\mathbf{p} - \mathbf{p}_{\text{RX},j_n}\| + \eta_{r,n}. \quad (45)$$

We assume M_r number of range estimates for the positioning.

Let $\hat{\theta}_m, \hat{\phi}_m$ denote the m -th azimuthal and elevation AoA measurements at the j_m -th RX. Therefore, the unit vector from the RX to the tag can be defined as

$$\hat{\mathbf{v}}_m = \begin{cases} [\cos \hat{\theta}_m, \sin \hat{\theta}_m]^\top, & D = 2 \\ [\sin \hat{\phi}_m \cos \hat{\theta}_m, \sin \hat{\phi}_m \sin \hat{\theta}_m, \cos \hat{\phi}_m]^\top, & D = 3. \end{cases} \quad (46)$$

We assume M_\angle number of angle estimates for the positioning. Note that the AoA $\hat{\theta}_{\text{B}}$ in Section III, which is the estimated angle in the antenna frame, should be converted to angles defined in a global reference frame, as depicted in Fig. 5. After AoA estimation and before positioning, a transformation matrix should be applied on $\hat{\mathbf{v}}_m$ to perform conversion from the antenna frame to global frame. We denote the transformation matrix by Ω and the unit directional vector in global frame will be $\hat{\mathbf{u}}_m = \Omega \hat{\mathbf{v}}_m$.

A. ML-based Positioning in Multi-static BN using Range and angle Measurements

We first introduce an ML-based positioning algorithm for multi-static BNs inspired from [36].

1) ML Formulation: As in (45), we assume that n -th range measurement is corrupted by zero-mean Gaussian noise with variance σ_n , i.e., $\eta_{r,n} \sim \mathcal{N}(0, \sigma_n)$. Therefore, the log likelihood function of the tag position given the n -th range estimate, after ignoring additive constants w.r.t. \mathbf{p} , is given by [34]

$$\ell_n^{(r)}(\mathbf{p}) = -\frac{(\hat{d}_n - \|\mathbf{p}_{\text{TX},i_n} - \mathbf{p}\| - \|\mathbf{p}_{\text{RX},j_n} - \mathbf{p}\|)^2}{2\sigma_n^2}. \quad (47)$$

Similarly, we assume that m -th angle measurement $\hat{\theta}_m$ is corrupted such that the estimated directional estimate $\hat{\mathbf{u}}_m$ follows von Mises-Fisher distribution with the mean direction \mathbf{u}_m and the concentration parameter κ_m . Hence,

$$\hat{\mathbf{u}}_m \sim \text{VMF}(\mathbf{u}_m, \kappa_m), \quad \text{and} \quad (48)$$

$$\mathbb{P}(\hat{\mathbf{u}}_m | \mathbf{u}_m, \kappa_m) = \frac{\kappa_m}{4\pi \sinh(\kappa_m)} \exp(\kappa_m \hat{\mathbf{u}}_m^\top \mathbf{u}_m). \quad (49)$$

Therefore, the log likelihood function of the tag position given the angle estimate $\hat{\theta}_m$, after ignoring additive constants w.r.t. \mathbf{p} , is given by

$$\ell_m^{(\angle)}(\mathbf{p}) = \log(\mathbb{P}[\hat{\mathbf{u}}_m | \mathbf{p}]) = \kappa_m \hat{\mathbf{u}}_m^\top \frac{\mathbf{p} - \mathbf{p}_{\text{RX},j_m}}{\|\mathbf{p} - \mathbf{p}_{\text{RX},j_m}\|}, \quad (50)$$

where we replace \mathbf{u}_m by $(\mathbf{p} - \mathbf{p}_{\text{RX},j_m})/\|\mathbf{p} - \mathbf{p}_{\text{RX},j_m}\|$.

Remark 1. We adopt a directional statistics approach because the natural parameter space of angles is not an Euclidean space, but a sphere. Therefore, a distribution

on the angles must account for the implicit periodicity of angles and must have a natural support over the unit sphere. The von Mises-Fisher distribution is the analog of the circular bi-variate normal distribution from the Euclidean space to the unit sphere. In fact, vMF distribution is equivalent to a bi-variate Gaussian distribution constrained onto a unit sphere in a D -dimensional space. The mean of such vMF distribution is the unit vector of the mean of the associated Gaussian distribution, and the reliability metric κ_m is associated to the variance of the Gaussian distribution. Refer to [30], [31] for more details.

The log likelihood function $\mathcal{L}(\mathbf{p})$ of the tag position given M_r -range and M_\angle -angle measurements is given by

$$\begin{aligned} \mathcal{L}(\mathbf{p}) &= \sum_{n=1}^{M_r} \ell_n^{(r)}(\mathbf{p}) + \sum_{m=1}^{M_\angle} \ell_m^{(\angle)}(\mathbf{p}), \\ &= \sum_{n=1}^{M_r} -\frac{(\hat{d}_n - \|\mathbf{p}_{\text{TX},i_n} - \mathbf{p}\| - \|\mathbf{p}_{\text{RX},j_n} - \mathbf{p}\|)^2}{2\sigma_n^2} \\ &+ \sum_{m=1}^{M_\angle} \kappa_m \hat{\mathbf{u}}_m^\top \frac{\mathbf{p} - \mathbf{p}_{\text{RX},j_m}}{\|\mathbf{p} - \mathbf{p}_{\text{RX},j_m}\|}. \end{aligned} \quad (51)$$

The tag's position can be estimated by maximizing the joint log likelihood function, i.e.,

$$\hat{\mathbf{p}}_{\text{ML}} = \underset{\mathbf{p} \in \mathbb{R}^D}{\text{argmax}} \mathcal{L}(\mathbf{p}). \quad (52)$$

Since the likelihood function is not a convex function, a brute force approach using the grid search can be employed. This approach includes (1) quantizing the region of interest into grid points with resolution ε_{ML} , (2) evaluating the log likelihood function on each point in the grid, and (3) selecting the grid point that maximizes the likelihood as a location estimate. While the grid search approach is guaranteed to provide a global optimal solution (up to the grid resolution), its computational cost increases inversely with ε_{ML} as $\mathcal{O}(D(M_r + M_\angle)\varepsilon_{\text{ML}}^{-D})$, where $\mathcal{O}(D(M_r + M_\angle))$ is the cost of evaluating the log-likelihood function.

For a practical deployment, we are interested in low complexity algorithms for real-time operations. Therefore, we introduce a gradient ascent-based heuristic algorithm to efficiently find the solution of (52).

2) ML Gradient Ascent with Line Search: To perform gradient ascent, we first obtain the gradients of $\mathcal{L}(\mathbf{p})$ as

$$\nabla \mathcal{L}(\mathbf{p}) \triangleq \frac{d}{d\mathbf{p}} \mathcal{L}(\mathbf{p}) \quad (53)$$

$$\begin{aligned} &= -\frac{1}{2} \sum_{n=1}^{M_r} \frac{1}{\sigma_n^2} \left[\left(\hat{d}_n - \|\mathbf{p}_{\text{TX},i_n} - \mathbf{p}\| - \|\mathbf{p}_{\text{RX},j_n} - \mathbf{p}\| \right) \right. \\ &\quad \left. \left(\frac{\mathbf{p}_{\text{TX},i_n} - \mathbf{p}}{\|\mathbf{p}_{\text{TX},i_n} - \mathbf{p}\|} + \frac{\mathbf{p}_{\text{RX},j_n} - \mathbf{p}}{\|\mathbf{p}_{\text{RX},j_n} - \mathbf{p}\|} \right) \right] \end{aligned} \quad (54)$$

$$\begin{aligned} &+ \sum_{m=1}^{M_\angle} \kappa_m \left(\frac{\mathbf{I}}{\|\mathbf{p} - \mathbf{p}_{\text{RX},j_m}\|} \right. \\ &\quad \left. - \frac{(\mathbf{p} - \mathbf{p}_{\text{RX},j_m})(\mathbf{p} - \mathbf{p}_{\text{RX},j_m})^\top}{\|\mathbf{p} - \mathbf{p}_{\text{RX},j_m}\|^3} \right) \hat{\mathbf{u}}_m. \end{aligned} \quad (55)$$

Since the log-likelihood function is not a convex function, the gradient ascent algorithm is not guaranteed to provide the optimal solution. Therefore, we introduce two

Algorithm 2 ML-based Gradient Ascent with Line Search

```

Input  $\{\hat{d}_n\}_{n=1}^{M_r}, \{\hat{\mathbf{u}}_m\}_{m=1}^{M_\angle}, \mathcal{S}, K$ 
1: Initializations  $\{\hat{\mathbf{p}}_{\text{ML},i}(0)\}_{i=1}^{5M_r}$ 
2: for  $i = 1$  to  $5M_r$  do
3:    $k \leftarrow 0$ 
4:   repeat
5:      $\mu_k^* \leftarrow \arg \max_{\mu_k \in \mathcal{S}} \mathcal{L}(\hat{\mathbf{p}}_{\text{ML},i}(k)) +$ 
6:      $\mu_k \nabla \mathcal{L}(\hat{\mathbf{p}}_{\text{ML},i}(k))$ 
7:      $\hat{\mathbf{p}}_{\text{ML},i}(k+1) \leftarrow \hat{\mathbf{p}}_{\text{ML},i}(k) + \mu_k^* \nabla \mathcal{L}(\hat{\mathbf{p}}_{\text{ML},i}(k))$ 
8:      $k \leftarrow k + 1$ 
8:   until  $\|\hat{\mathbf{p}}_{\text{ML},i}(k) - \hat{\mathbf{p}}_{\text{ML},i}(k-1)\| \leq \varepsilon_{\text{ML}}$  or  $k = K_{\text{ML}}$ 
9: end for
10:  $i^* \leftarrow \arg \max_{i \in \{1, \dots, 5M_r\}} \mathcal{L}(\hat{\mathbf{p}}_{\text{ML},i}(k))$ 
Output  $\hat{\mathbf{p}}_{\text{ML}} \leftarrow \hat{\mathbf{p}}_{\text{ML},i^*}(k)$ 

```

features in the gradient ascent to improve the possibility of reaching to the global maximum.

(a) Multiple initializations: The gradient ascent iterations are initialized at the center, two vertices and two co-vertices of the ellipse associated to each TX-RX pair (see Fig.2). This results in $5M_r$ initialization points denoted by $\hat{\mathbf{p}}_{\text{ML},i}(0)$, $i = 1, \dots, 5M_r$. An independent instance of the gradient ascent algorithm is executed for each initial point.

(b) Multiple step-sizes in each gradient ascent iteration: For each instance of the gradient ascent, the estimate is updated at each iterations by selecting a step-size from a fixed set \mathcal{S} which maximizes the log-likelihood function. Specifically,

$$\hat{\mathbf{p}}_{\text{ML},i}(k+1) = \hat{\mathbf{p}}_{\text{ML},i}(k) + \mu_k^* \nabla \mathcal{L}(\hat{\mathbf{p}}_{\text{ML},i}(k)), \quad (56)$$

$$\text{where, } \mu_k^* = \arg \max_{\mu_k \in \mathcal{S}} \mathcal{L}(\hat{\mathbf{p}}_{\text{ML},i}(k) + \mu_k \nabla \mathcal{L}(\hat{\mathbf{p}}_{\text{ML},i}(k))). \quad (57)$$

Dynamically selecting the step-size in each iteration of gradient ascent is also called gradient ascent with line search. At the end of each instance of the gradient ascent, the position that maximizes the likelihood is selected as the location estimate. As for the stopping criterion, we either use ε_{ML} as a predefined position accuracy threshold or a maximum number of iterations K_{ML} . We summarize this algorithm, subsequently called Gradient Ascent with Line Search, in Algorithm 2.

Given $5M_r$ initializations, $|\mathcal{S}|$ evaluations of the log-likelihood functions in each iteration, and $\mathcal{O}(D(M_r + M_\angle))$ complexity for the evaluation of the log-likelihood function, the total computational cost of the proposed ML-based gradient ascent with line search is given by $\mathcal{O}(D(M_r + M_\angle)M_r|\mathcal{S}|K_{\text{ML}})$.

Note that, compared to ML-based grid search, the gradient search reduces the complexity by avoiding the exponential dependence on the number of dimensions D . This reduction in the complexity comes as a cost of the possibility of a sub-optimal solution and an additional linear dependence on M_r .

B. Iterative Re-weighted Least Squares (IRLS)

In this section, we propose an iterative positioning approach called IRLS. While several prior works consider the IRLS algorithm [37], [39], [41], they primarily focus on either range- or angle-only position estimation. We instead

introduce the IRLS method that uses both range and angle estimates for multi-static positioning. Accordingly, we first formulate a pseudo-linear problem for multi-static positioning using range and angle measurements. We then introduce iterative weight updates, and finally, summarize the algorithm and discuss its computational complexity.

1) Pseudo-linear Formulation [37]: Assuming the noise $\eta_{r,n} \ll \hat{d}_n$, by re-arranging and squaring (45), we get

$$\frac{1}{\varphi_{r,n}} [2(\mathbf{p}_{RX,jn} - \mathbf{p}_{TX,in})^\top \quad 2\hat{d}_n] \begin{bmatrix} \mathbf{p} \\ \|\mathbf{p} - \mathbf{p}_{RX,jn}\| \end{bmatrix} = 1. \quad (58)$$

where

$$\varphi_{r,n} = \hat{d}_n^2 - \|\mathbf{p}_{TX,in} - \mathbf{p}_{RX,jn}\|^2 + 2(\mathbf{p}_{RX,jn} - \mathbf{p}_{TX,in})^\top \mathbf{p}_{RX,jn}. \quad (59)$$

Collecting (58) for all M_r range measurements, we define

$$\Phi_r = [\Phi_{r,1}^\top, \Phi_{r,2}^\top, \dots, \Phi_{r,M_r}^\top]^\top \in \mathbb{R}^{M_r \times (D+N_{RX})}, \quad (60)$$

$$\Phi_{r,n} = \frac{1}{\varphi_{r,n}} [2(\mathbf{p}_{RX,jn} - \mathbf{p}_{TX,in})^\top, \mathbf{0}_{j_n-1}^\top, 2\hat{d}_n, \mathbf{0}_{N_{RX}-j_n}^\top]. \quad (61)$$

Similarly, assuming low angle measurement errors, we have

$$[\mathbf{I}_D - \hat{\mathbf{u}}_m] \begin{bmatrix} \mathbf{p} \\ \|\mathbf{p} - \mathbf{p}_{RX,jm}\| \end{bmatrix} = \mathbf{p}_{RX,jm} \triangleq \varphi_{\angle,m}. \quad (62)$$

Collecting (62) for all M_\angle angle measurements, we define

$$\Phi_\angle = [\Phi_{\angle,1}^\top, \dots, \Phi_{\angle,M_\angle}^\top]^\top \in \mathbb{R}^{M_\angle \times (D+N_{RX})}, \quad (63)$$

$$\Phi_{\angle,m} = [\mathbf{I}_D, \mathbf{0}_{D \times (j_m-1)}, -\hat{\mathbf{u}}_m, \mathbf{0}_{D \times N_{RX}-j_m}^\top], \quad (64)$$

$$\varphi_\angle = [\varphi_{\angle,1}^\top, \dots, \varphi_{\angle,M_\angle}^\top]^\top \in \mathbb{R}^{M_\angle \times 1}. \quad (65)$$

Finally, let

$$\boldsymbol{\Upsilon} = [\mathbf{p}^\top, \|\mathbf{p} - \mathbf{p}_{RX,1}\|, \dots, \|\mathbf{p} - \mathbf{p}_{RX,N_{RX}}\|]^\top, \quad (66)$$

$$\Phi = [\Phi_r^\top, \Phi_\angle^\top]^\top \in \mathbb{R}^{(M_r+DM_\angle) \times (D+N_{RX})}, \quad (67)$$

$$\varphi = [\mathbf{1}_{M_r}^\top, \varphi_\angle^\top]^\top \in \mathbb{R}^{(M_r+DM_\angle) \times 1}. \quad (68)$$

From (58) and (62), (66)-(68) can be collectively written as

$$\Phi \boldsymbol{\Upsilon} = \varphi. \quad (69)$$

To estimate the tag position, we need to estimate $\boldsymbol{\Upsilon}$ using a least square solution given Φ and φ . This provides a pseudo-linear² formulation of the multi-static positioning problem, given the range and angle measurements. Furthermore, this formulation can also be extended to include the measurements from multiple methods simply by stacking more rows in the matrix Φ and φ .

Remark 2. In addition to using both range and angle measurements, our IRLS formulation differs from the prior work in another way. All rows corresponding to the range measurements in (69) are scaled such that their respective elements in φ is 1. From (58), note that $\varphi_{r,n}$ depends on the locations of the TXs and RXs, and \hat{d}_n . While most prior work focused on simulations which resulted in comparable $\varphi_{r,n}$ across all measurements, our experience with the real-world prototype showed that, in practice, $\varphi_{r,n}$ varies drastically across measurements. Hence, solving (69) without the scaling by $\varphi_{r,n}$ would give artificially high importance to the measurements with high $\varphi_{r,n}$. This problem is further exacerbated if n -th range measurement is an outlier resulting in high \hat{d}_n^2 , which would add higher weight to an outlier measurement! Therefore, we tackle this problem (highlighted by our experimental setup) by

²(69) is a pseudo-linear formulation because the parameters defined in $\boldsymbol{\Upsilon}$ are not independent variables, but have non-linear dependency between them.

simply scaling (58) by $\varphi_{r,n}$ such that the right hand side is one.

While a least squares solution solves (69), from a practical perspective, there are two key challenges:

- Errors in the measurements: (69) does not account for the possible errors in the range and angle measurements due to signal noise and multipaths in the propagation environment.

- Validity of estimated $\boldsymbol{\Upsilon}$: The least square solution of (69) does not enforce the dependency within $\{\boldsymbol{\Upsilon}_i\}_{i=1}^{D+N_{RX}}$. Specifically, the solution $\hat{\boldsymbol{\Upsilon}}$ is only valid if

$$\|[\hat{\boldsymbol{\Upsilon}}]_{1:D} - \mathbf{p}_{RX,j}\| = [\hat{\boldsymbol{\Upsilon}}]_{D+j}, \forall j \in \{1, \dots, N_{RX}\}. \quad (70)$$

In the following, we introduce two methods to tackle these two challenges.

2) Iterative Re-Weighted Least Square: The formulation in (69) assumes all measurements to have same importance. However, an error in one measurement may distort the estimate. Therefore, we introduce a measure of reliability for each measurement.

We define a weight vector $\mathbf{w} \in \mathbb{R}^{M_r+DM_\angle}$ as the weights assigned to each row of (69). Then, with $\mathbf{W} = \text{Diag}\{\mathbf{w}\}$, we solve

$$\hat{\boldsymbol{\Upsilon}} = \min_{\boldsymbol{\Upsilon}} (\boldsymbol{\varphi} - \Phi \boldsymbol{\Upsilon})^\top \mathbf{W} (\boldsymbol{\varphi} - \Phi \boldsymbol{\Upsilon}), \quad (71)$$

which results in

$$\hat{\boldsymbol{\Upsilon}} = (\sqrt{\mathbf{W}} \Phi)^\dagger \sqrt{\mathbf{W}} \boldsymbol{\varphi}. \quad (72)$$

The position estimate is then given by

$$\hat{\mathbf{p}}_{IRLS} = [\hat{\boldsymbol{\Upsilon}}]_{1:D}. \quad (73)$$

To estimate the position $\hat{\mathbf{p}}_{IRLS}$ robustly, our goal is to select the weights \mathbf{w}_r and \mathbf{w}_\angle such that the outliers are assigned lower weight. For that, we use an iterative approach as follows:

- 1) Initialize the weight vector by $\mathbf{w} = \mathbf{1}_{M_r+DM_\angle}$.
- 2) Estimate $\hat{\boldsymbol{\Upsilon}}$ using (72).
- 3) Estimate the residual errors $\mathbf{e} = |\Phi \boldsymbol{\Upsilon} - \boldsymbol{\varphi}|$.
- 4) Define \mathbf{w} such that $\mathbf{w}_i = (\mathbf{e}_i^2 + \varepsilon_{IRLS})^{-1}$.
- 5) Repeat 2-4 for K number of iterations,

where ε_{IRLS} prevents excessively large weights and ensures stability. We emphasize here that while we set same initial weights for all measurements, in practice, there are other approaches using measurement metrics. For instance, the measurements from the tag packets with higher signal strength quality or lower bit error rate can be assigned higher initial weights. However, given that IRLS does not guarantee an optimal solution, it is not possible to definitively conclude the best choice for the initial weights.

3) Ensuring Validity of the Estimate: The solution of (72) assumes that the elements of $\boldsymbol{\Upsilon}$ are independent. However, the estimated $\hat{\boldsymbol{\Upsilon}}$ is valid only if (70) is satisfied. To ensure that this constraint is satisfied, we use a second stage least squares solution [37], [39] to project $\hat{\boldsymbol{\Upsilon}}$ on to feasible cone of (70). Let $\boldsymbol{\eta}_{IRLS}$ represent the error between the estimated $\hat{\boldsymbol{\Upsilon}}$ and the true $\boldsymbol{\Upsilon}$ i.e. $\hat{\boldsymbol{\Upsilon}} = \boldsymbol{\Upsilon} + \boldsymbol{\eta}_{IRLS}$. We define $\boldsymbol{\Upsilon}_2 = \mathbf{p}_2 \odot \mathbf{p}_2$ as the unknown of the second stage least squares and correspondingly \mathbf{p}_2 as the tag position estimate after projection. Then,

$$\boldsymbol{\Upsilon}_2 = [\hat{\boldsymbol{\Upsilon}}]_{1:D} \odot [\hat{\boldsymbol{\Upsilon}}]_{1:D} - 2[\boldsymbol{\eta}_{\text{IRLS}}]_{1:D} \odot [\hat{\boldsymbol{\Upsilon}}]_{1:D}. \quad (74)$$

Squaring (70) yields,

$$\begin{aligned} \mathbf{1}^\top \boldsymbol{\Upsilon}_2 - [\hat{\boldsymbol{\Upsilon}}]_{D+j}^2 - 2\mathbf{p}_{\text{RX},j}^\top [\hat{\boldsymbol{\Upsilon}}]_{1:D} + \|\mathbf{p}_{\text{RX},j}\|^2 \\ = -2[\hat{\boldsymbol{\Upsilon}}]_{D+j} [\boldsymbol{\eta}_{\text{IRLS}}]_{D+j} - 2\mathbf{p}_{\text{RX},j}^\top [\boldsymbol{\eta}_{\text{IRLS}}]_{1:D}, \end{aligned} \quad (75)$$

for $j = \{1, \dots, N_{\text{RX}}\}$. In (74)-(75), we use $\boldsymbol{\Upsilon} = \hat{\boldsymbol{\Upsilon}} - \boldsymbol{\eta}_{\text{IRLS}}$ and eliminated the second-order error terms. Consequently, (74)-(75) are recast in matrix form as $\boldsymbol{\Phi}_2 \boldsymbol{\Upsilon}_2 = \boldsymbol{\varphi}_2$, where

$$\boldsymbol{\Phi}_2 = [\mathbf{I}_D, \mathbf{1}_D, \dots, \mathbf{1}_D]^\top \in \mathbb{R}^{(D+N_{\text{RX}}) \times D}, \quad (76)$$

$$\boldsymbol{\varphi}_2 = \hat{\boldsymbol{\Upsilon}} \odot \hat{\boldsymbol{\Upsilon}} + \begin{bmatrix} \mathbf{0}_D \\ 2\mathbf{p}_{\text{RX},1}^\top [\hat{\boldsymbol{\Upsilon}}]_{1:D} - \|\mathbf{p}_{\text{RX},1}\|^2 \\ 2\mathbf{p}_{\text{RX},2}^\top [\hat{\boldsymbol{\Upsilon}}]_{1:D} - \|\mathbf{p}_{\text{RX},2}\|^2 \\ \vdots \\ 2\mathbf{p}_{\text{RX},N_{\text{RX}}}^\top [\hat{\boldsymbol{\Upsilon}}]_{1:D} - \|\mathbf{p}_{\text{RX},N_{\text{RX}}}\|^2 \end{bmatrix} \quad (77)$$

Then, we find \mathbf{p}_2 such that

$$\hat{\mathbf{p}}_2 = \arg \min_{\mathbf{p}_2 \in \mathbb{R}^D} \|\boldsymbol{\Phi}_2 \boldsymbol{\Upsilon}_2 - \boldsymbol{\varphi}_2\|^2, \quad (78)$$

which results in the solution

$$\hat{\boldsymbol{\Upsilon}}_2 = \hat{\mathbf{p}}_2 \odot \hat{\mathbf{p}}_2 = \boldsymbol{\Phi}_2^\dagger \boldsymbol{\varphi}_2. \quad (79)$$

Therefore, the final position estimate from the IRLS algorithm can be given as

$$\hat{\mathbf{p}}_{\text{IRLS}} = \text{sign}([\hat{\boldsymbol{\Upsilon}}]_{1:D}) \odot \sqrt{\boldsymbol{\Phi}_2^\dagger \boldsymbol{\varphi}_2}. \quad (80)$$

Note that (80) improves upon the estimate (73) by fulfilling the constraint introduced in (70).

4) Algorithm Complexity: The computation for IRLS algorithm is dominated by the pseudo-inverse operation defined on line 3 of the algorithm. Given that the dimensions of $\boldsymbol{\Phi}$ is $(M_r + DM_\angle) \times (D + N_{\text{RX}})$, the complexity of the pseudo-inverse operation is $\mathcal{O}(D(M_r + DM_\angle)^2)$. Therefore, the total complexity of the IRLS algorithm is given by $\mathcal{O}(KD(M_r + DM_\angle)^2)$.

V. Numerical Results

In this section, we present the simulated performance of the proposed estimation and localization algorithms.

A. Simulation Setup

Four TXs are located at the coordinates $(0, 0)$, $(0, 6)$, $(-18, 6)$, and $(-18, 0)$ m within the room. The RX, equipped with an antenna array with $N_a = 4$ half-wavelength-spaced elements, is positioned at $(-9, 3)$ m. 25 tags are placed uniformly in the region $(x, y) \in [-18, 0] \times [0, 6]$ m. All TXs, RX and tags are assumed to have same height, making the entire deployment a 2D deployment.

Scatterers are uniformly distributed in the same region as the tag positions. We assume $L_1, L_2 = 3$ number of scatterers in the environment. Further, we generate 50 OFDM symbols, with 40 subcarriers uniformly spaced at 1 MHz, according to (24). We further contaminate the OFDM symbols by Gaussian noise $\mathbf{v}^{(n)} \sim \mathcal{N}(0, \sigma_v^2)$ such that the SNR = $\frac{\|\mathcal{H}_{B,n}^{(n)}\|}{\sigma_v^2}$ is 5 dB.

B. Range-Angle Estimation Performance

We evaluate joint range-angle estimation methods from Section III: 2D FFT, 2D MUSIC, SRAE with $T_{\min}^{\text{SRAE}} = 0.5$, and JRAC with $T_{\min}^{\text{JRAC}} = 0.2$ and $T_{\max}^{\text{JRAC}} = 0.6$. We also add a range-only estimation using IR First [10] as a baseline to emulate a single-antenna RX. For all algorithms, we use same sets \mathcal{T} and $\boldsymbol{\Theta}$ with $G_\tau = 4096$, $G_\theta = 128$. This ensures that performance and runtime of proposed algorithms and IR First are fairly compared.

Fig. 3 compares the performance of these five algorithms in terms of the absolute range estimation error $|d - \hat{d}|$ and the absolute angle estimation error $|\hat{\theta} - \theta|$. Fig. 3a shows that the range-angle estimation algorithms outperforms the range-only baseline. This indicates the benefit of separating the multipath components along the spatial dimensions to improve the range estimates. Among the range-angle estimation algorithms, both Fig. 3a and 3b shows (a) JRAC outperforming 2D FFT and 2D MUSIC, and (b) SRAE under-performing 2D FFT and 2D MUSIC. JRAC outperforms due to the clustering step which considers a multiple paths as a unit instead of evaluating individual paths as done by 2D FFT and 2D MUSIC. Furthermore, SRAE under-performs the joint methods due to its stage-wise architecture. In theory, since delay and angle are coupled in multipath environments, joint algorithms can separate them more accurately.

C. Positioning Performance

The benefit of positioning based on joint range and angle measurements from synthetically generated dataset, compared to range-only measurements, is illustrated in Fig. 3c. In a two-dimensional positioning scenario, range-only localization requires a minimum of three ellipses corresponding to three TXs to estimate a tag position. In contrast, when the RX is equipped with an antenna array and the AoA estimates are available, the tag position can be determined using as few as one range and one angle measurements from a single TX. Fig. 3c further shows that even with a sufficient number of TXs, equipping the RX with a ULA to enable AoA estimation significantly improves positioning accuracy. Specifically, with three TXs, range-only measurements result in an average positioning error of approximately 6m, which is reduced to about 2m when AoA estimation at the RX is feasible.

VI. Experimental Results

We conduct the experimental evaluation on a custom-built wireless testbed deployed in an enclosed lab space (metal walls). The testbed spans an area of 20 m \times 7 m and includes four TXs, a single multi-channel RX, and 100 custom-designed semi-passive backscatter tags distributed across the area. The TXs and RX operate without any clock synchronization, reflecting a realistic multi-static architecture without clock distribution. The experimental setup is given in Fig. 4.

Each TX uses an ADRV9361-Z7035 chip connected to a dipole antenna and continuously broadcasts an OFDM waveform with 39.36 MHz bandwidth centered at

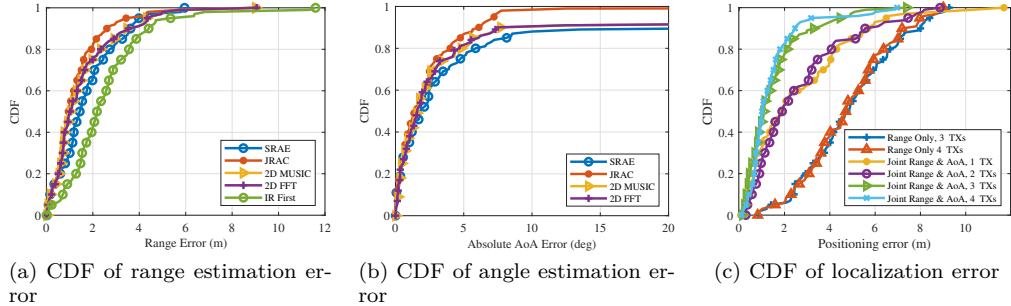


Fig. 3. (a)-(b) Range and angle estimation errors using simulation data: Range-AoA estimation methods have higher ranging accuracy compared to the range-only method IR-First. Joint methods such as JRAC achieves higher ranging and angle estimation accuracy compared to the stage-wise method, SRAE. (c) Using AoA for localization with various number of TXs: We compare positioning accuracy using range only and joint range-angle measurements from the synthetic data. We consider SNR= 5 dB, $L_1 = L_2 = 3$ scatterers, 1D MUSIC for the range estimation and 2D MUSIC for joint range and angle estimation. Localization uses ML-based Gradient Ascent with Line Search.

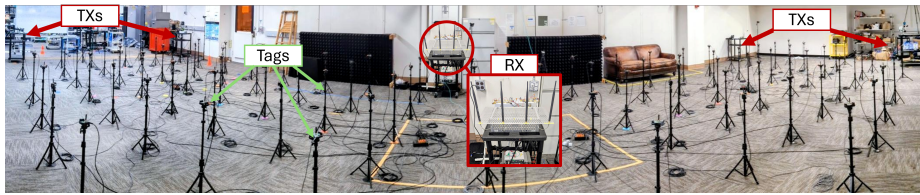


Fig. 4. The experimental setup of a large-scale BN consisting of 4 TXs, 1 RX with 4-element antenna array, and 100 tags in an enclosed lab. The walls with metal surface and the ground introduce significant multipath in the channel.

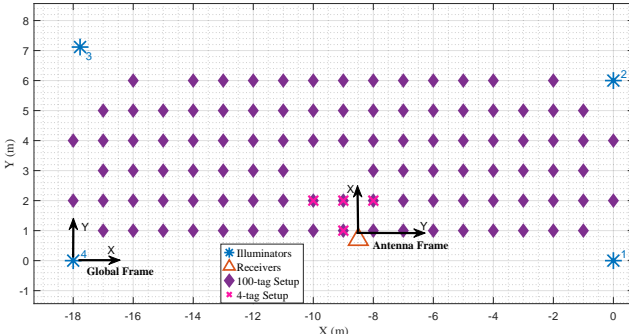


Fig. 5. Schematic of the experimental setup consisting 4 TXs, 1 RX with 4-element antenna array, and 100 tags. The positive-X direction in the antenna frame denotes the broadside direction of the receiver antenna array.

897.5 MHz. The OFDM waveform contains 41 subcarriers spaced at 960 kHz, following the design principles in [10].

The backscatter tags have the semi-passive architecture described in [10]. Each tag transmits one 100-bit packet of duration 4.8 ms at a uniformly random time within every 300 ms window [11]. Tags modulate the incident OFDM carrier using a square-wave switching mechanism and apply a frequency shift of 45 MHz to separate the backscatter signal from the carrier, which prevents interference with the direct signal from the TX.

The receiver is built around a USRP X440 with eight RF channels. A 4-element half-wavelength-spaced custom ULA feeds into 4 RF diplexers, which split each antenna feed into two bands containing: (a) carrier signal from the direct TX-RX path, and (b) backscatter signal from the TX-tag-RX path. This configuration produces eight input streams to the USRP. Since USRP X440 lacks internal amplification, we add external LNAs with 20 dB gain each, which boosts the SNR of weak backscatter signals.

The USRP samples all eight streams at an ADC rate of 61.44 MSps and sends them to the host computer for processing. I/Q processing follows the steps described in [10]. The RX estimates CFRs for all streams, estimates the phase and timing references from the four carrier channels, and computes the range and angle estimates from the four backscatter channel estimates of each detected tag. Then, the estimated tag direction in the antenna frame is transformed to the world frame as explained in (46). For the topology illustrated in Fig. 5, the transformation matrix is $\Omega = \begin{bmatrix} 0 & 1 \\ 1 & 0 \end{bmatrix}$. Finally, the range and angle estimates for each tag using the carrier signals from all 4 TXs are used to estimate the position of the tags. We evaluate two scenarios as shown in Fig. 5.

- 4-tag setup: This setup presents an ideal condition with high SNR and few collisions. We keep four tags close to the RX on and capture 1.2 seconds of continuous samples.
- 100-tag setup: This setup emulates a realistic deployment with low SNR and dense deployment. We keep all 100 tags on and capture 15 seconds of continuous samples to ensure sufficient observations for evaluation.

In both scenarios, the TXs transmit continuously and the RX records raw I/Q samples for processing. We evaluate four range-angle estimation algorithms described in Section III: (a) 2D FFT, (b) 2D MUSIC, (c) SRAE with $T_{\min}^{\text{SRAE}} = 0.5$, and (d) JRAC with $T_{\min}^{\text{JRAC}} = 0.2$ and $T_{\max}^{\text{JRAC}} = 0.6$. Similar to Fig. 3a, we also add a range-only estimation using IR First [10] as a baseline to emulate a single-antenna RX setup. For all algorithms, we use same sets \mathcal{T} and Θ with $G_\tau = 4096$ and $G_\theta = 128$. This ensures that performance and runtime of proposed algorithms and

IR First are fairly compared.

In Fig. 6a, we show the CDF of absolute ranging error $|\hat{d} - d|$ for the 4-tag scenario. The 2D FFT and IR First algorithms maintain performance similar to the simulated results in Fig. 3a. In contrast, the 2D MUSIC, SRAE, and JRAC methods exhibit noticeable degradation in ranging accuracy. This degradation occurs because these algorithms rely on a MUSIC-based step for delay estimation. MUSIC assumes a well-defined signal and noise subspace, which becomes unreliable in real-world multipath environments. Coherent multipath components and uncertainty in the number of subspaces significantly reduce the robustness of MUSIC for delay estimation, as noted in prior studies [45], [46].

In Fig. 6b, we present the CDF of absolute AoA estimation error. Unlike the range results, MUSIC-based algorithms outperform FFT-based methods for angle estimation. This improvement occurs because, at high SNR, spatial subspaces are more separable than delay subspaces, even in multipath environments. The ULA provides spatial diversity, which allows MUSIC to exploit subspace decomposition for high-resolution angle estimation. In contrast, FFT-based methods suffer from coarse grid resolution and spectral leakage, which limit angular accuracy. Therefore, while MUSIC struggles with delay estimation, it remains effective for AoA estimation under high-SNR conditions.

In Fig. 6d and 6e, we present the CDF of absolute ranging and AoA errors in 100-tag setup. While the relative performance of various methods remain similar to that of the 4-tag setup, the overall performance of the estimation algorithms drops substantially. This is due to three possible reasons: (a) low SNR in 100-tag setup, (b) additional multipath introduced by the tags when not transmitting a packet. We observe that CIRs of the carrier and backscatter channels in the 100-tag setup are significantly more cluttered than in the 4-tag setup for the same TX, RX, and the tag. This shows that there are more multipaths in the environment with 100 tags, indicating that when the tags are on and not modulating a packet, they indeed act as (unmodulated) reflectors, due to the semi-passive architecture. Unlike passive tags where the tag antenna is connected to a matched load (and therefore absorbing incident RF signals) when not modulating, semi-passive tags have their antenna always connected to a mismatched load [47]. Therefore, even when the tags are not modulating, the signals are reflected with a phase shift, resulting in additional multipaths. A potential resolution would be the use of multi-state RF front-ends to “mute” the tags that are not transmitting packets, by introducing a matched or low-reflection state (e.g. [48]). Furthermore, in Fig. 6e, we also observe the longer tail in the angle estimation error. The longer tails denote the fundamental limit of the angle estimation in the end-fire region of the ULA, in which many tags are located (refer to Fig. 5).

Table I presents the average runtime required to compute a range and angle estimate from each tag packet

TABLE I
Computational complexity and Runtime of Joint Range and Angle Estimation Methods for $N_{\text{sym}} = 98$ OFDM symbols.

Estimation Method	Computational Complexity	Average Runtime (ms)
SRAE	$\mathcal{O}(G_\tau N_s^3 + G_\theta N_a^3)$	55
JRAC	$\mathcal{O}(G_\tau N_s^3 + G_\tau G_\theta N_s N_a)$	475
2D MUSIC	$\mathcal{O}(G_\tau G_\theta N_a^2 N_s^2 + N_a^3 N_s^3)$	10380
2D FFT	$\mathcal{O}(G_\tau G_\theta \log(G_\tau G_\theta))$	2038

TABLE II
Runtime of Positioning Methods

Positioning Method	Computational Complexity	Runtime (ms)	
		4-tag	100-tag
ML Grid Search	$\mathcal{O}(D(M_r + M_\angle)\varepsilon_{\text{ML}}^{-D})$	4670	22802
ML Gradient Ascent with Line Search	$\mathcal{O}(D(M_r + M_\angle)M_r \mathcal{S} K_{\text{ML}})$	500	15818
IRLS	$\mathcal{O}(DK(M_r + DM_\angle)^2)$	38	51

using the four algorithms. The SRAE and JRAC methods outperform the others by orders of magnitude, achieving near real-time processing capability. In contrast, 2D FFT and 2D MUSIC incur significantly higher computational costs due to their reliance on complex FFT and expensive grid searches, respectively. This difference in runtime becomes critical for scalability in dense deployments. While the relative accuracy and the runtime of different range-angle estimation algorithms varies, ultimately the metric of interest is the overall positioning quality using the respective range and angle estimates.

We evaluate the positioning performance of two optimization methods described in Section IV: (a) ML-based Gradient Ascent with Line Search proposed in Algorithm 2 with $\sigma_n, \kappa_n = 1$ and the line search step sizes $\mathcal{S} = \{0.001, 0.01, 0.1, 1\}$. (b) IRLS proposed in Section IV-B with $\varepsilon_{\text{IRLS}} = 10^{-6}$. The analysis uses range-angle estimates obtained from four algorithms: JRAC, SRAE, 2D MUSIC, and 2D FFT. Fig. 6c and 6f shows the CDF of positioning error for the 4-tag and 100-tag datasets. The 4-tag dataset achieves substantially better positioning accuracy than the 100-tag dataset. This improvement is expected because the 4-tag scenario represents a simplified environment with high SNR, whereas the 100-tag scenario introduces lower SNR and heavy multipath, which degrade localization accuracy. Among the range-angle estimation algorithms, 2D FFT combined with ML-based positioning achieves the lowest positioning error. This result aligns with the robustness of 2D FFT on real-world data and the optimality of ML-based estimation. Interestingly, the two low-complexity algorithms proposed in this paper—JRAC and SRAE—deliver positioning accuracy comparable to 2D FFT when paired with IRLS. This finding demonstrates that reducing computational complexity in range-angle estimation does not necessarily compromise positioning quality, making JRAC and SRAE practical for large-scale deployments.

Table II reports the average runtime for computing position estimates using ML Gradient Ascent with Line Search and IRLS for both datasets. It also includes a brute-force baseline that searches the ML objective over a grid with 5 cm granularity. The results show that ML-based methods scale with the number of tags and the

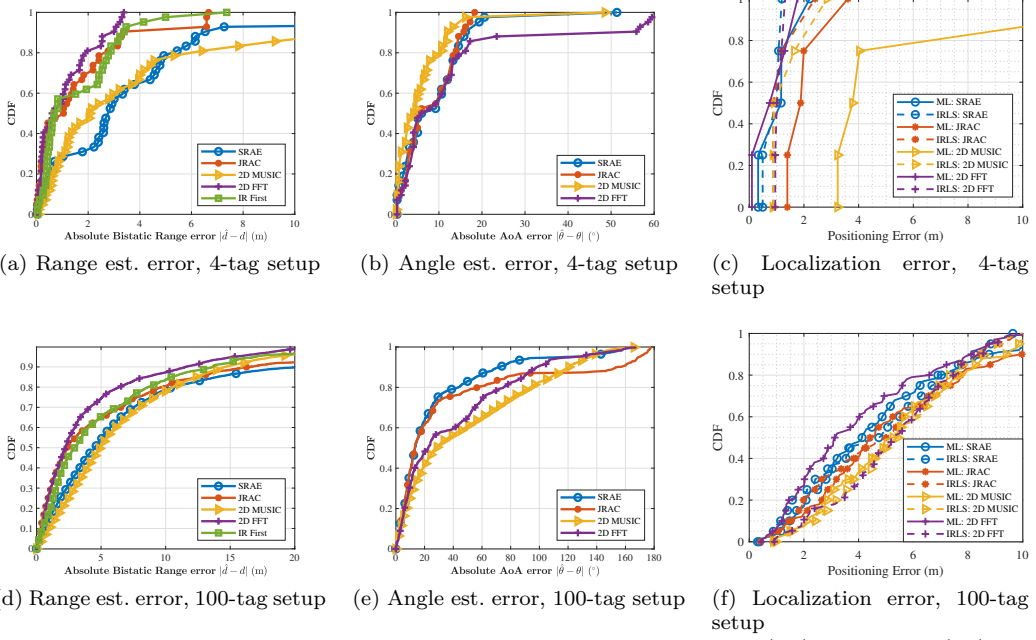


Fig. 6. Joint range and angle estimation, and localization error on experimental setup with (a-c) 4 tags, and (d-f) 100 tags. (c,f) $A : B$ denotes the positioning method A is applied to the ranges and AoAs which are estimated by method B . ML method denotes ML-based Gradient Ascent with Line Search.

number of measurements per tag, both of which are higher in the 100-tag dataset. In contrast, IRLS requires only the inversion of a tall matrix with fixed rank, so its runtime grows much more slowly. Overall, ML with gradient ascent demands significantly more computational time: at least $10\times$ higher than IRLS in the 4-tag setup and $300\times$ higher in the 100-tag setup. These results highlight that while ML and IRLS achieve comparable positioning accuracy, IRLS offers a clear advantage in scalability.

Overall, even though the ranking of range-angle estimation algorithms differs between range and angle accuracy, the ultimate metric of interest is positioning quality. Our results show that JRAC and SRAE, combined with IRLS, deliver the best trade-off between accuracy and computational efficiency. This makes them strong candidates for practical multi-static localization systems.

VII. Conclusion

In this work, we introduced the JRAC and SRAE methods for real-time joint range–AoA estimation in multistatic BNs. These two methods achieve range and angle measurement accuracy comparable to FFT- and subspace-based baselines, while significantly reducing computational complexity. Building on these measurements, we investigated tag localization using both ML and IRLS algorithms. Our experimental results revealed that an unmodified IRLS approach, as commonly adopted in prior literature, can assign artificially high weights to outlier measurements, leading to degraded localization performance. To address this limitation, we proposed a scaling scheme that effectively mitigates the impact of outliers. We further demonstrated that the scaled IRLS algorithm achieves localization accuracy comparable to

brute-force search on the ML criterion, while significantly reducing computational complexity. This reduction enables practical real-time tag localization, making the proposed approach well suited for use in large-scale, time-critical BN deployments.

References

- [1] K. Zheng, R. Xu, J. Mei, H. Yang, L. Lei, and X. Wang, “Ambient IoT toward 6G: Standardization, potentials, and challenges,” *IEEE Access*, vol. 12, pp. 146 668–146 677, 2024.
- [2] N. Van Huynh, D. T. Hoang, X. Lu, D. Niyato, P. Wang, and D. I. Kim, “Ambient backscatter communications: A contemporary surv.” *IEEE Commun. Surveys & Tutorials*, vol. 20, no. 4, pp. 2889–2922, 2018.
- [3] M. M. Butt, N. R. Mangalvedhe, N. K. Pratas, J. Harrebek, J. Kimionis, M. Tayyab, O.-E. Barbu, R. Ratasuk, and B. Vejgaard, “Ambient IoT: A missing link in 3GPP IoT devices landscape,” *IEEE Internet of Things Mag.*, vol. 7, no. 2, pp. 85–92, 2024.
- [4] Global, EPC, “EPC radio-frequency identity protocols class-1 generation-2 UHF RFID protocol for communications at 860 MHz–960 MHz,” GS1, 2008.
- [5] J. D. Griffin and G. D. Durgin, “Complete Link Budgets for Backscatter-Radio and RFID Systems,” *IEEE Antennas Propag. Mag.*, vol. 51, no. 2, pp. 11–25, 2009.
- [6] H. G. Wang, C. X. Pei, and C. H. Zhu, “A link analysis for passive UHF RFID system in LoS indoor environment,” *Int. Conf. Wireless Commun., Netw. Mobile Comput.*, pp. 1–7, 2008.
- [7] J. Kimionis, A. Bletsas, and J. N. Sahalos, “Increased range bistatic scatter radio,” *IEEE Trans. Commun.*, vol. 62, no. 3, pp. 1091–1104, 2014.
- [8] G. Vougioukas, S.-N. Daskalakis, and A. Bletsas, “Could battery-less scatter radio tags achieve 270-meter range?” in *IEEE wireless power transfer Conf.*, 2016, pp. 1–3.
- [9] P. N. Alevizos, K. Tountas, and A. Bletsas, “Multistatic Scatter radio sensor networks for extended coverage,” *IEEE Trans. Wireless Commun.*, vol. 17, no. 7, pp. 4522–4535, 2018.
- [10] T. E. Abrudan, K. Patel, J. Kimionis, T. Esmaeilbeig, E. Kampianakis, S. D. Liyanaarachchi, and M. Eggleston, “Next-generation backscatter networks for integrated communications and RF sensing,” *arXiv preprint arXiv:2509.12954*, 2025.

[11] K. Patel, J. Zhang, J. Kimionis, L. Kampianakis, M. S. Eggleston, and J. Du, "Analyzing the scalability of bi-static backscatter networks for large scale applications," *IEEE J. of Radio Freq. Identification*, vol. 9, pp. 6–16, 2025.

[12] E. Kampianakis, J. Kimionis, K. Tountas, C. Konstantopoulos, E. Koutroulis, and A. Bletsas, "Wireless environmental sensor networking with analog scatter radio and timer principles," *IEEE Sensors J.*, vol. 14, no. 10, pp. 3365–3376, 2014.

[13] G. Vannucci, A. Bletsas, and D. Leigh, "A software-defined radio system for backscatter sensor networks," *IEEE Trans. Wireless Commun.*, vol. 7, no. 6, pp. 2170–2179, 2008.

[14] D. Bharadia, K. R. Joshi, M. Kotaru, and S. Katti, "BackFi: High throughput WiFi backscatter," *ACM SIGCOMM Comput. Commun. Rev.*, vol. 45, no. 4, pp. 283–296, 2015.

[15] B. Kellogg, V. Talla, S. Gollakota, and J. R. Smith, "Passive Wi-Fi: Bringing low power to Wi-Fi transmissions," *USENIX Symp. on Networked Syst. Design and Implementation*, 2016.

[16] P. Zhang, D. Bharadia, K. Joshi, and S. Katti, "HitchHike: Practical backscatter using commodity WiFi," *Proc. ACM Conf. embedded network sensor Syst. CD-ROM*, pp. 259–271, 2016.

[17] P. Zhang, C. Josephson, D. Bharadia, and S. Katti, "FreeRider: Backscatter communication using commodity radios," *Proc. Int. Conf. Emerg. Netw. Experiments and Technologies*, pp. 389–401, Nov. 2017.

[18] B. Kellogg, A. Parks, S. Gollakota, J. R. Smith, and D. Wetherall, "Wi-Fi backscatter: Internet connectivity for RF-powered devices," *ACM SIGCOMM Comput. Commun. Rev.*, vol. 44, no. 4, pp. 607–618, Aug. 2014.

[19] V. Talla, M. Hessar, B. Kellogg, A. Najafi, J. R. Smith, and S. Gollakota, "LoRa backscatter: Enabling the vision of ubiquitous connectivity," *Proc. ACM Interactive, Mobile, Wearable and Ubiquitous Technologies*, vol. 1, no. 3, pp. 105:1–105:24, Sep. 2017.

[20] S. Wang, Y. Yan, F. Han, Y. Tian, Y. Ding, P. Yang, and X.-Y. Li, "MultiRider: Enabling multi-tag concurrent OFDM backscatter by taming in-band interference," in *Proc. Annu. Int. Conf. Mobile Syst., Appl. and Services*, 2024, pp. 292–303.

[21] K. Skyvalakis, E. Giannelos, E. Andrianakis, and A. Bletsas, "Elliptical DoA estimation & localization," *IEEE J. of Radio Freq. Identification*, vol. 6, pp. 394–401, 2022.

[22] M. Vestakis, P. N. Alevizos, G. Vougioukas, and A. Bletsas, "Multistatic Narrowband Localization in Backscatter Sensor Networks," in *IEEE Int. Workshop Signal Process. Advances Wireless Commun.*, 2018, pp. 1–5.

[23] J. Jiang, J. Wang, Y. Chen, S. Tong, P. Xie, Y. Liu, and Y. Liu, "Willow: Practical WiFi backscatter localization with parallel tags," in *Proc. Annu. Int. Conf. Mobile Syst., Appl. and Services*, 2024, pp. 265–277.

[24] J. Kim, J. Chun, and S. Song, "Joint range and angle estimation for FMCW MIMO radar and its application," *arXiv preprint arXiv:1811.06715*, 2018.

[25] I. Jaafar, R. Amara, H. Boujemâa, and M. Siala, "Joint angle and delay estimation of point sources," in *Int. Conf. Electron. Circuits and Syst. IEEE*, 2005, pp. 1–5.

[26] Y. Schröder and L. Wolf, "InPhase: Phase-based ranging and localization," *ACM Trans. Sensor Netw.*, vol. 18, no. 2, 2022.

[27] X. Xu, T. Huang, X. Kuai, and Y.-C. Liang, "Joint localization and signal detection for ambient backscatter communication systems," *IEEE Trans. Wireless Commun.*, vol. 23, no. 10, pp. 14 437–14 451, 2024.

[28] M. Wu and C. Hao, "Super-Resolution ToA and AoA estimation for OFDM radar systems based on compressed sensing," *IEEE Trans. Aerosp. and Electron. Syst.*, vol. 58, no. 6, pp. 5730–5740, 2022.

[29] M. Kotaru, K. Joshi, D. Bharadia, and S. Katti, "SpotFi: Decimeter level localization using WiFi," in *Proc. ACM Conf. special interest group data Commun.*, 2015, pp. 269–282.

[30] K. V. Mardia and P. E. Jupp, *Directional Statistics*. Wiley Series in Probability and Statistics, 1999.

[31] T. E. Abrudan, Z. Xiao, A. Markham, and N. Trigoni, "Underground incrementally deployed magneto-inductive 3-D positioning network," *IEEE Trans. Geosci. Remote Sens.*, vol. 54, no. 8, pp. 4376–4391, 2016.

[32] S. Wang, B. R. Jackson, and R. Inkol, "Performance characterization of AoA geolocation systems using the von Mises distribution," in *IEEE Veh. Technol. Conf.*, 2012, pp. 1–5.

[33] H. Naseri and V. Koivunen, "A Bayesian algorithm for distributed network localization using distance and direction data," *IEEE Trans. Signal Inf. Process. over Netw.*, vol. 5, no. 2, pp. 290–304, 2018.

[34] K. Panwar, P. Babu, and P. Stoica, "Maximum likelihood algorithm for time-delay based multistatic target localization," *IEEE Signal Process. Lett.*, vol. 29, pp. 847–851, 2022.

[35] F. Perez-Cruz, C.-K. Lin, and H. Huang, "BLADE: A universal, blind learning algorithm for ToA localization in NLoS channels," in *IEEE Globecom Workshops*, 2016, pp. 1–7.

[36] C. Geng, T. E. Abrudan, V.-M. Kolmonen, and H. Huang, "Experimental study on probabilistic ToA and AoA joint localization in real indoor environments," in *IEEE Int. Conf. Commun.*, 2021, pp. 1–6.

[37] Y. T. Chan and K. C. Ho, "A simple and efficient estimator for hyperbolic location," *IEEE Trans. signal Process.*, vol. 42, no. 8, pp. 1905–1915, 1994.

[38] F. Ma, L. Yang, M. Zhang, and F.-C. Guo, "TDoA source positioning in the presence of outliers," *IET Signal Process.*, vol. 13, no. 7, pp. 679–688, 2019.

[39] R. Amiri, F. Behnia, and H. Zamani, "Asymptotically efficient target localization from bistatic range measurements in distributed MIMO radars," *IEEE Signal Process. Lett.*, vol. 24, no. 3, pp. 299–303, 2017.

[40] P. Varshney, P. Babu, and P. Stoica, "Outlier-robust multistatic target localization," *IEEE Signal Process. Lett.*, 2025.

[41] T. Abrudan, H. Claussen, and V.-M. Kolmonen, "Positioning system and method," Nov. 19 2024, US Patent 12,146,975.

[42] O. Kanhere, S. Goyal, M. Beluri, and T. S. Rappaport, "Target localization using bistatic and multistatic radar with 5G NR waveform," *IEEE Veh. Technol. Conf.*, pp. 1–7, 2021.

[43] N. Decarli and D. Dardari, "RFID and radar localization: A position error bound analysis," in *IEEE Int. Conf. Commun. Workshops*, 2013, pp. 37–41.

[44] H. Marom, Y. Bar-Shalom, and B. Milgrom, "Bistatic Radar Tracking With Significantly Improved Bistatic Range Accuracy," *IEEE Trans. Aerosp. and Electron. Syst.*, vol. 59, no. 1, pp. 52–62, Feb. 2023.

[45] T.-J. Shan, M. Wax, and T. Kailath, "On spatial smoothing for direction-of-arrival estimation of coherent signals," *IEEE Trans. Acoustics, Speech, and Signal Process.*, vol. 33, no. 4, pp. 806–811, 1985.

[46] R. Schmidt, "Multiple emitter location and signal parameter estimation," *IEEE Trans. Antennas and Propag.*, vol. 34, no. 3, pp. 276–280, 1986.

[47] A. Bletsas, A. G. Dimitriou, and J. N. Sahalos, "Improving backscatter radio tag efficiency," *IEEE Trans. Microw. Theory and Techniques*, vol. 58, no. 6, pp. 1502–1509, 2010.

[48] J. Kimionis and M. M. Tentzeris, "RF tag front-end design for uncompromised communication and harvesting," in *IEEE RFID Technol. and Appl. Conf.*, 2014, pp. 109–114.